UNIVERSITY OF CALIFORNIA,
IRVINE

Fluorescence based adaptive optics and multidimensional fluorescence microscopy

DISSERTATION

submitted in partial satisfaction of the requirements
for the degree of

DOCTOR OF PHILOSOPHY

in Biomedical Engineering

by

Simon W. Leemans

Dissertation Committee:
Professor Enrico Gratton, Chair
Associate Professor Michelle Digman
Assistant Professor Daryl Preece

2020

DEDICATION

To my wife Tara and my family: Wim, Annette, Nelia, Eline, Richie, Nico, Susan, Mike, Rachel, Brian, Alex.

TABLE OF CONTENTS

LIST OF FIGURES

LIST OF TABLES

Page

ACKNOWLEDGMENTS

A special thank you to my advisor, Enrico Gratton, for your unwavering support and faith in your students. You have been a fantastic mentor and teacher of physics, biology, and engineering. Thank you for giving me freedom to explore and helping me grow into a better scientist and person.

To my mentor, Sasha Dvornikov, who taught me to stop and think carefully before I act in the lab. To do things right the first time, whether that means machining a new part or just rethinking the entire idea to come out with a better solution.

I would also like to thank both Enrico Gratton and Michelle Digman for organizing and hosting all of the LFD and USIBR workshops over the years. It was an incredible learning experience on many levels.

Thank you to all of my committee members that have given me valuable feedback and input and helped make my projects successful: Michelle Digman, Vasan Venugopalan, Eric Potma, Gary Chanan, and Daryl Preece.

Thank you to Vasan Venugopalan for giving me the opportunity to be part of the NSF IGERT BEST program and giving me financial support. Thank you for the many interesting discussions, and introducing me to the wide world of biophotonics. Thank you also to Bruce Tromberg for helping to shape my view of biophotonics, photochemistry, and biomedical engineering.

To my inspiring lab mates and mentors: Austin Lefebvre, Balam Benitez, Dean Nguyen, Suman Ranjit, Leonel Malacrida, Francesco Palomba, Belen Torrado, Milka Stakic, Lorenzo Scipioni, Giulia Tedeschi, Alex Vallmitjana, Rachel Cinco, Nik Hedde, Christoph Gohlke, Yukai Huang, Andrew Trinh, Michael Murata, Sara Sameni, Ning Ma, Emma Mah, Hongtao Chen, you all have been a blast to work with and I hope there will be many more coffee breaks to come.

Thank you to all my friends for all the surfing, mountain biking, road tripping, BBQ's, camping, fun times and parties, and making my experience at UCI unforgettable.

I would also like to thank Sean Kuan from the Plikus lab for providing the K14-GFP mouse skin sample, Tam Vu for rescuing the brain sample, Jerome Ballesta and Axiom Optics for loaning us a Haso4 wavefront sensor. A lot of the work in my dissertation was supported by NIH P41-GM103540 and NIH P50-GM076516, and I was supported by NSF IGERT BEST Fellowship DGE-1144901.

VITA

Simon W. Leemans

EDUCATION

Doctor of Philosophy in Biomedical Engineering — **2020**
University of California, Irvine — *Irvine, CA*

Masters of Science in Biomedical Engineering — **2019**
University of California, Irvine — *Irvine, CA*

Bachelor of Science in Applied Physics — **2015**
University of California, Santa Cruz — *Santa Cruz, CA*

RESEARCH EXPERIENCE

Graduate Research Assistant — **2016–2020**
Laboratory for Fluorescence Dynamics, UC Irvine — *Irvine, CA*

Associate Scientist — **2015–2016**
Alameda Applied Sciences Corporation — *San Leandro, CA*

Research Support Student — **2013–2015**
SLAC National Accelerator Laboratory — *Menlo Park, CA*

ATLAS Intern — **2012**
Lawrence Berkeley National Laboratory — *Berkeley, CA*

Chemistry Laboratory Assistant — **2010**
UC Berkeley — *Berkeley, CA*

TEACHING EXPERIENCE

Group Leader Annual LFD Workshop — **2018, 2019**
UC Irvine — *Irvine, CA*

Project Leader USIBR — **2018, 2019**
UC Irvine — *Irvine, CA*

Student Mentor — **2014**
SLAC National Accelerator Laboratory — *Menlo Park, CA*

AWARDS AND FUNDING

NSF IGERT fellow **2017–2019**
UC Irvine *Irvine, CA*

REFEREED JOURNAL PUBLICATIONS

Krishnan, M., Velas, K., Leemans, S. Metal Plasma Thruster for small satellites. **2020**
Journal of Propulsion and Power. doi: https://doi.org/10.2514/1.B37603

Mlynczak, J., ..., Leemans, S. *et al.* Practical application of cross correlation technique to measure jitter of master-oscillator-power-amplifier (MOPA) laser system. **2014**
Opto-Electronics Review. doi: https://doi.org/10.2478/s11772-014-0200-4

PUBLICATIONS UNDER REVIEW

S.W. Leemans, A. Dvornikov, T. Gallagher, E. Gratton. Three-dimensional adaptive optics network advances multiphoton imaging of tissue to multi-millimeter depths. **2020**
(Manuscript under review.)

T. Gallagher*, S. W. Leemans*, *et al.* (*Co-first author). Fluorescence lifetime and hyperspectral microscopy track metabolism in Pseudomonas aeruginosa biofilms. **2020**
(Manuscript under review)

T. Gallagher, ... S. Leemans, *et al.* LC-MS detection of antibiotic agents in sputum from persons with cystic fibrosis. **2020**
(Manuscript under review.)

PUBLISHED ABSTRACTS

Leemans, S. W., Dvornikov, A., Gallagher, T., Gratton, E. AO-DIVER Advances the Depth Limits of Multiphoton Microscopy in Scattering Media. **2020**
Biophysical Journal, 118(3), 307a.

Leemans S.W., Gratton E. Adaptive optics in strongly scattering samples. **2019**
Biophys J. 2019; 116(3, Suppl 1): 441a, 2181-Pos

Leemans S.W., Dvornikov A., Gratton E. Adaptive optics in deep tissue microscopy. **2018**
Biophys J. 2018; 114(3, Suppl 1): 533a, 2638-Pos.

SOFTWARE

HyperFluo `https://github.com/swleemans/HyperFluo`
Python program for unmixing of pure species in fluorescence lifetime and hyperspectral images.

AO DIVER module `https://github.com/swleemans/AODIVER`
Delphi user interface built on top of SimFCS (https://www.lfd.uci.edu/globals/) for 3D AO microscopy and hardware interfacing with Boston Micromachines deformable mirrors. Also includes Matlab code for simulations.

ABSTRACT OF THE DISSERTATION

Fluorescence based adaptive optics and multidimensional fluorescence microscopy

By

Simon W. Leemans

Doctor of Philosophy in Biomedical Engineering

University of California, Irvine, 2020

Professor Enrico Gratton, Chair

Studying the structure and interactions of molecules and cells in their native environments has always been a challenge in the life sciences. When an organism of interest is physically out of reach or invisible to the naked eye, scientists have historically turned to reductionist experiments that first isolate the organism from a complex environment and then study the bulk signal from a large population of cells in tissue or in bacterial colonies. However, the structure, function, and interactions of a population of cells can vary at a subpopulation and even single-cell level. Non-invasive tools that can study a population in relevant conditions, such as in tissue, capable of resolving single-cells in a large region of interest are necessary to improve treatment of disease and understanding of physiological phenomena.

Microscopy – in particular multiphoton fluorescence microscopy – holds enormous potential to discover new science by elucidating biological properties with subcellular resolution. When paired with adaptive optics, multiphoton microscopy can image deep into highly scattering tissue, resolving structures at previously inaccessible depths. The biochemical composition of a sample can be determined with fluorescence lifetime microscopy and hyperspectral microscopy, giving information about cell state and metabolism. Image correlation spectroscopy and single molecule tracking methods can yield information about the dynamic sample properties such as transport mechanisms and diffusion of genetically encoded fluorescent proteins.

The work presented in this thesis is separated into three chapters. The first chapter describes the development of a novel deep tissue multiphoton microscope, the AO DIVER, which uses a network of guide stars to perform millimeter-scale 3D adaptive optics imaging and enable millimeter-scale imaging. In the second chapter, the deformable mirror used in the AO DIVER is used to create a high speed 3D scanning instrument, capable of scanning axially and laterally at rates rates of up to 40 kHz. Finally, in the third chapter, a program for simultaneous unmixing of hyperspectral and lifetime fluorescence images is described and implemented in Pseudomonas aeruginosa biofilms, elucidating a depth dependent physiological change in bacterial biofilms.

Chapter 1

The AO DIVER: deep tissue imaging with light shaping and index matched detection

Co-authors:

T. Gallagher, A. Dvornikov, E. Gratton

1.1 Abstract

Multiphoton microscopy (MPM) can non-invasively measure the dynamic biochemical properties throughout biological samples and has the potential to accelerate clinical research with advances in deep tissue imaging. In most samples, the imaging depth of MPM is limited to fractions of a millimeter due to blurring caused by refractive index mismatching throughout tissue and background fluorescence, overshadowing the signal in conventional MPM. To overcome these challenges, we developed a novel 3-D adaptive optics (AO) system that uses an interpolated network of endogenous guide stars to focus laser light more efficiently into highly scattering samples. The synergistic combination of our AO system with DIVER detection technology enables millimeter-scale imag-

ing with diffraction-limited resolution. The system improves the signal to noise ratio by a factor of 5, $\sim$0.4 mm deep in mouse skin and a factor of 2, $\sim$2 mm deep in mouse brain, resolving tissue architecture at previously inaccessible depths.

1.2 Introduction

Deep tissue imaging has the potential to transform biology and medicine by visualizing the interactions between cells and their environments on a tissue-wide scale. One of the most promising imaging modalities for non-invasive deep tissue imaging with submicron resolution is multiphoton microscopy (MPM) [2, 3, 4]. MPM can detect a wide range of optical biosensors to measure biochemical properties throughout tissue while maintaining sub-micron resolution. By using a pulsed infrared laser to image deep into samples, MPM causes less phototoxicity and suffers less from image blurring compared to the shorter wavelengths of light aused in confocal microscopy [2, 3, 4]. Scattering and absorption of the infrared excitation light used in MPM are significantly smaller in comparison to the shorter visible wavelengths used in confocal microscopy [2]. Thicker sections of tissue can be imaged due to the improved depth penetration of longer wavelengths, allowing more accurate measurements of morphology and physical properties [4]. Even in highly scattering samples, the spatio-temporal focusing requirements of nonlinear signal generation mitigate the blurring effect of scattering [5]. In most fresh and fixed tissues, image blurring and background noise limit conventional multiphoton microscopes to depths of hundreds of microns [4, 5, 6]. The availability of fluorescently tagged proteins and endogenous fluorophores also means there is often no need for histological preparation [7], so the biochemical environment of the cells in the tissue can be better preserved. Optical clearing of tissue improves imaging depths but requires chemical treatment with organic solvents or ionic detergents [8], changing the physical and chemical properties of tissues.

In contrast to the conventional epi-detection geometry, the DIVER (Deep Imaging Via Enhanced

photon Recovery) microscope [9] detects fluorescence light through the sample – on the opposite side of the objective– dramatically cutting the intensity of top-surface fluorescence [1]. The wide area DIVER detector also improves signal detection efficiency as a function of the depth, due to the increasing numerical aperture [1]. The DIVER detector mitigates the problem of signal acquisition deep in scattering tissue samples [10]. However, tissue heterogeneity distorts the propagation of excitation light, resulting in image blurring that grows with the depth of the imaging plane.

To enhance focusing of laser light into scattering samples and extend the imaging range of MPM, we integrated a deformable mirror in the excitation path of the microscope– the AO DIVER. We developed a wavefront optimization method based on the downhill Simplex method [11, 12] to simultaneously optimize all n actuators in the deformable mirror, leveraging the nonlinear dependence of multiphoton excitation fluorescence on intensity as a measure of the wavefront error [13, 14, 15]. In contrast to other indirect wavefront sensing approaches [16, 17], our optimization based approach makes no assumptions about orthogonality and allows the deformable mirror to explore a wider range of spatial frequencies.

Our single-point AO method is ideal for imaging deep in highly scattering samples. Other approaches such as image-based optimization [18, 19] and direct wavefront sensing [20] require relatively high quality images to work. Direct wavefront sensing requires a spatially coherent, bright guide star, but in scattering samples, the guide star signal is deteriorated by the high-frequency phase structure of the sample ([21] and supplemental figures in [22]).

Using a single point correction with the downhill Simplex algorithm at each region of interest is a fast ($\sim$15-65 seconds) and highly efficient method to improve imaging resolution in depth and minimize losses to stray light. The DIVER detector recovers photons that would otherwise be lost to scattering in the sample, and the transmission geometry minimizes the influence of out-of-focus fluorescence light. In turn, the improved detection efficiency and specificity give high fidelity feedback to the AO optimization algorithm, which further improves the resolution and brightness of the image.

To expand the technique to enable three-dimensional imaging on millimeter scales with a single deformable mirror, we developed a user interface to generate a network of endogenous guide stars. The guide stars are used to create single point wavefront corrections that are interpolated throughout the sample, correcting wavefront aberrations throughout the volume at high speeds.

1.3 Results

1.3.1 Using nonlinear guide stars to create a 3-dimensional network of adaptive optics corrections

To improve the focusing of excitation light using a high-speed ($\sim$40kHz) segmented MEMS deformable mirror (Boston Micromachines Hex-111, Cambridge MA) we implemented a feedback loop (Fig. 1.1a) that uses the intensity of a guide star as a measure of the validity of a wavefront correction. In the AO DIVER microscope, the guide star can be a fluorescent object of any size that produces two- or three-photon excitation fluorescence (2PEF or 3PEF) or has some optical nonlinearity that results in second-harmonic generation (SHG) or third-harmonic generation (THG). In this article, we only show 2PEF results; however, the technique works just as well for 3PEF and has the most robust performance for SHG and THG. The strong performance is due to the photo-stability of coherent nonlinear processes, whereas 2PEF and 3PEF typically experience higher rates of photobleaching, which confounds the optimization process.

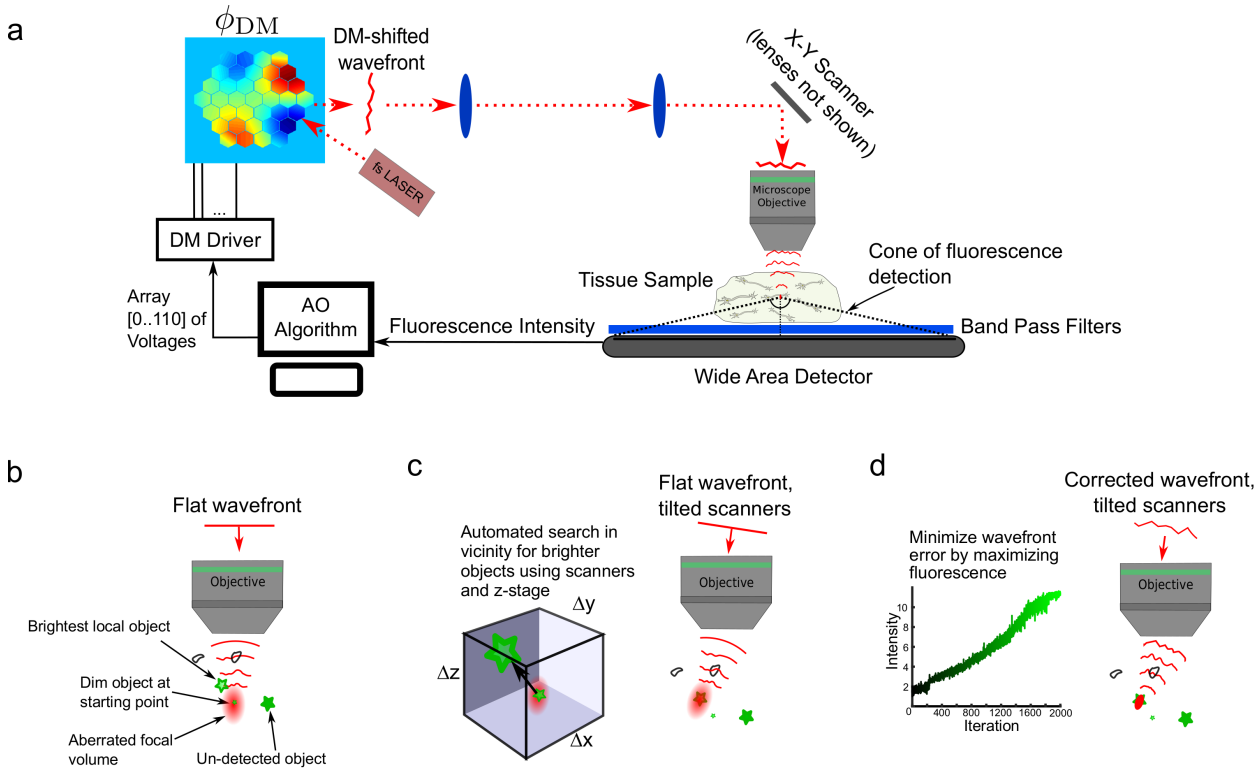

Figure 1.1: **a.** The AO DIVER feedback loop uses the fluorescence intensity to minimize phase aberrations. ϕ_{DM} is the phase shift introduced to the excitation laser beam by the deformable mirror (DM). **b.** A workflow was developed to help users create a 3D network of AO corrections without translational distortions. First the beam is parked on an object by clicking on the image. **c.** An automated search algorithm then moves the beam around a small volume to ensure that the light is focused on a local maximum, to minimize tip, tilt and defocus in the final deformable mirror setting. **d.** Fluorescence based optimization minimizes the focal volume, increasing the image brightness and resolution. The plot in panel d of intensity vs. iteration is a typical wavefront optimization trace.

The phase and amplitude aberrations introduced by the sample play a significant role in determining the spatial extent and intensity of the point spread function. The characteristics of the point spread function can be described by a composite phase function at the back focal plane ϕ_{BF} of the objective, made up of system aberrations, ϕ_{SYS}, and the phase shift from the deformable mirror, ϕ_{DM}. The sample induced phase shifts, ϕ_{Sample} can also be mapped onto ϕ_{BF}, giving a function $\phi_{BF} = \phi_{SYS} + \phi_{DM} + \phi_{Sample}$. Diffraction-limited imaging is attained when the deformable mirror flattens the phase function ϕ_{BF}.

In a steady-state system, the 2PEF intensity scales proportionally to the square of the intensity of the excitation light, $I_{ex}(\vec{r}, \phi_{BF})$, and the concentration of the fluorophores, $C(\vec{r})$, as well as a constant α, which accounts for absorption cross-section, quantum efficiency, and detection efficiency [23],

$$\langle I_f \rangle \approx \alpha \int_V I_{ex}^2(\vec{r}, \phi_{BF}) C(\vec{r}) dV. \tag{1.1}$$

The calculation of the average fluorescence intensity is simplified by the assumption that the total intensity of the excitation pulse is the laser power P (constant) divided over a volume V, which is changed by the phase at the back focal plane of the system, ϕ_{BF}. The total number of fluorophores that contribute to the detected fluorescence intensity is determined by the size of the excitation focal volume, $V(\phi_{BF})$, and the concentration of fluorophores inside the volume of observation,

$$\langle I_f \rangle \propto \left(\frac{P}{V(\phi_{BF})} \right)^2 V(\phi_{BF}) C(x,y,z) \tag{1.2}$$

$$\rightarrow I_f \propto P^2 \frac{C(x,y,z)}{V(\phi_{BF})}. \tag{1.3}$$

The optimal mirror configuration is determined by the spatial distribution of fluorescent molecules, $C(x,y,z)$, and the focus size and shape, $V(\phi_{BF})$. The dependence of the fluorescence intensity on the concentration and the focal volume means that the algorithm minimizes the volume of illumination and improves optical resolution. However, it can also translate the center of the focus to the location with the highest fluorophore concentration. If this occurs, the deformable mirror can take the shape of the three translational Zernike modes – tip, tilt and defocus.

One of the challenges with 3-dimensional adaptive optics is that each region of the sample has a different wavefront correction if there is any refractive index variation throughout the sample. The AO correction is generally valid for some finite area, known as the isoplanatic patch, over which the wavefront aberration does not change significantly. To produce an AO-corrected z-stack in the

most time-efficient manner, we developed a program that allows the microscope user to create a network of AO corrections. To fully cover the volume of interest, the program linearly interpolates wavefront corrections between guide stars. For corrections ϕ_A and ϕ_B at z_A and z_B respectively, the shape of the mirror, ϕ at a location z is given by the linear relation,

$$\phi = \phi_A + \frac{z - z_A}{z_B - z_A}(\phi_B - \phi_A). \tag{1.4}$$

The interpolation of wavefronts in equation 1.4 and the relationship in equation 1.3 highlight an important feature in implementing the 3D adaptive optics system. If there is a difference in the tip-tilt-defocus modes between z_A or z_B, the deformable mirror continuously shifts the center of the field of view between the two guide stars. The presence of translational modes distorts the images, making objects appear artificially larger or smaller.

Two steps ensure that the AO system is only optimizing the phase function, and not the spatial location of the focus. First, the beam is required to be parked on a local maximum. To do this, we programmed an automated search algorithm that traverses through a small region around the starting point ($\Delta x, \Delta y, \Delta z$ in Fig. 1.1c) to find the brightest point in the region using the XY-scanners and Z-translation stage before starting the AO optimization algorithm. The search algorithm parks the beam on the true center of the guide star, so that the DM does not erroneously translate the field of view. Translation is also constrained during the optimization routine. The program periodically checks the mirror configuration for the presence of translational modes in the mirror setting using a Shack-Hartmann wavefront sensor (Haso 4 Imagine Optic, Orsay, France) . If more than 2 µm of translation are detected, the optimization routine is terminated. The field of view is then re-centered by the addition of equal and opposite translational modes.

Another challenge in wavefront interpolation is that highly heterogeneous samples require more frequent and varied adaptive optics corrections. For optically clear samples, the wavefront deformation is mainly due to index mismatching between the sample and the immersion medium, which

results in spherical aberrations [24]. In this case, only a top and bottom correction are needed for good imaging quality throughout the sample. However, for more complex samples with discrete scattering particles throughout the sample, the wavefront deformation varies more quickly and must be corrected at smaller intervals. For linear interpolation to work, the DM setting must also closely follow the true phase correction. For this reason, corrections are done from the top-down, starting with a flat wavefront at the top and taking relatively small steps in Z to ensure that the phase perturbation from step to step is small. The optimization is also initialized with the previous step's correction. In addition, the starting search space is limited to about $\lambda/3$ per actuator.

1.3.2 System Aberration Correction

To demonstrate the improvement in both image brightness and resolution as a result of maximizing the fluorescence intensity, we imaged a field of sub-diffraction 500 nm beads spin-coated onto a microscope slide. Setting the deformable mirror to a flat surface (factory setting) resulted in visible astigmatism in the image on the left of Fig 1.2a. After optimizing the intensity of the center bead until convergence, the astigmatism is resolved. To quantify the improvement in resolution images are first binarized to select individual fluorescent beads. We then use the 3D Gaussian-Lorentzian model for a two-photon excitation point spread function to fit the beads and calculate the lateral beam waist as well as the Rayleigh length (also known as depth of field). There is good agreement between the theoretical model and the actual focal shape (Fig. 1.2b), with beads in the AO off images giving a mean R-squared goodness-of-fit of $\sim$0.75. The images with AO correction give a near-perfect R-squared of $\sim$0.96. On average, the intensity of the beads is increased by a factor of 5. The lateral resolution is improved $\sim$30% from approximately 1.4 µm to a diffraction-limited beam waist of 1.0 µm (Fig. 1.2c). The axial resolution is also improved from approximately 7.0 µm to a diffraction-limited Rayleigh length of 4.4 µm.

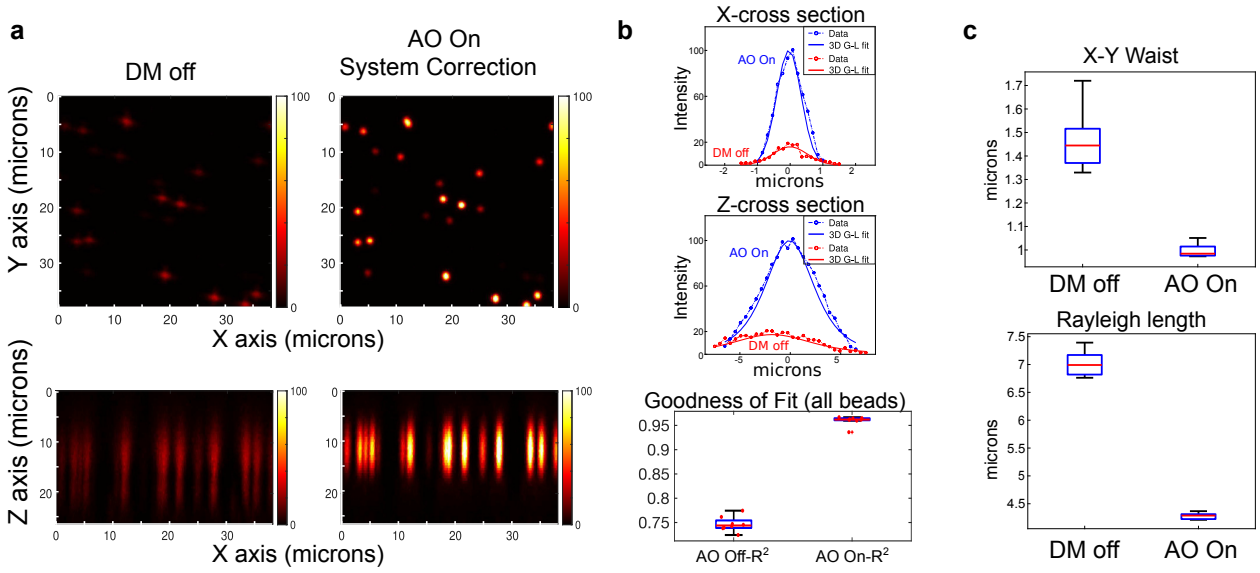

Figure 1.2: **a.** Images of 500nm yellow-green fluorescent microspheres acquired using 780nm excitation light, 20x 0.4NA Olympus objective. The top left image is an X-Y image of the flat field of beads with the deformable mirror switched off, and at the bottom left is a maximum intensity projection along the Y-direction. After optimizing the intensity, the improvement in image quality is evident in the two images on the right of panel a. **b.** Representative cross-sections across fluorescent beads in the X and the Z directions show the improvement in intensity as well as the fit to the Gaussian-Lorentzian (G-L) model. **c.** The improvement in lateral (x-waist) and axial (z-waist) resolution, averaged across 8 fluorescent beads in the field of view that meet intensity criteria in the AO off image. The mean R-squared for the volumetric fit of each bead without AO correction is 0.75, with AO on, the G-L model fits significantly better with R-square of 0.96. Pairwise T-test gives $P<0.05$ for all points in panel c with $N = 8$ beads.

1.3.3 K14-GFP transgenic mouse skin

The performance of the AO DIVER is demonstrated in a skin sample from a transgenic mouse with GFP (green fluorescent protein) tagged keratinocytes (K-14). Images are acquired through the fat side of the skin through approximately 400 µm of tissue. Skin is a highly scattering sample, with significant variations in the refractive index throughout the tissue, leading to a blurry image (Fig. 1.3a). At these depths, the isoplanatic patch is relatively small, on the order of ~ 20 µm, so lateral wavefront corrections are performed at eight different locations 1.3d, using the cell-encoded GFP as guide stars. Each of the deformable mirror settings are saved, and 3 frames of images are

acquired and averaged. The series of 8 corrected images are compiled into a single image (AO on) by maximum intensity projection in Fig. 1.3b. In Fig. 1.3c the intensity across the inset is plotted, showing that the signal to noise ratio is improved from about 5.8 to over 26.

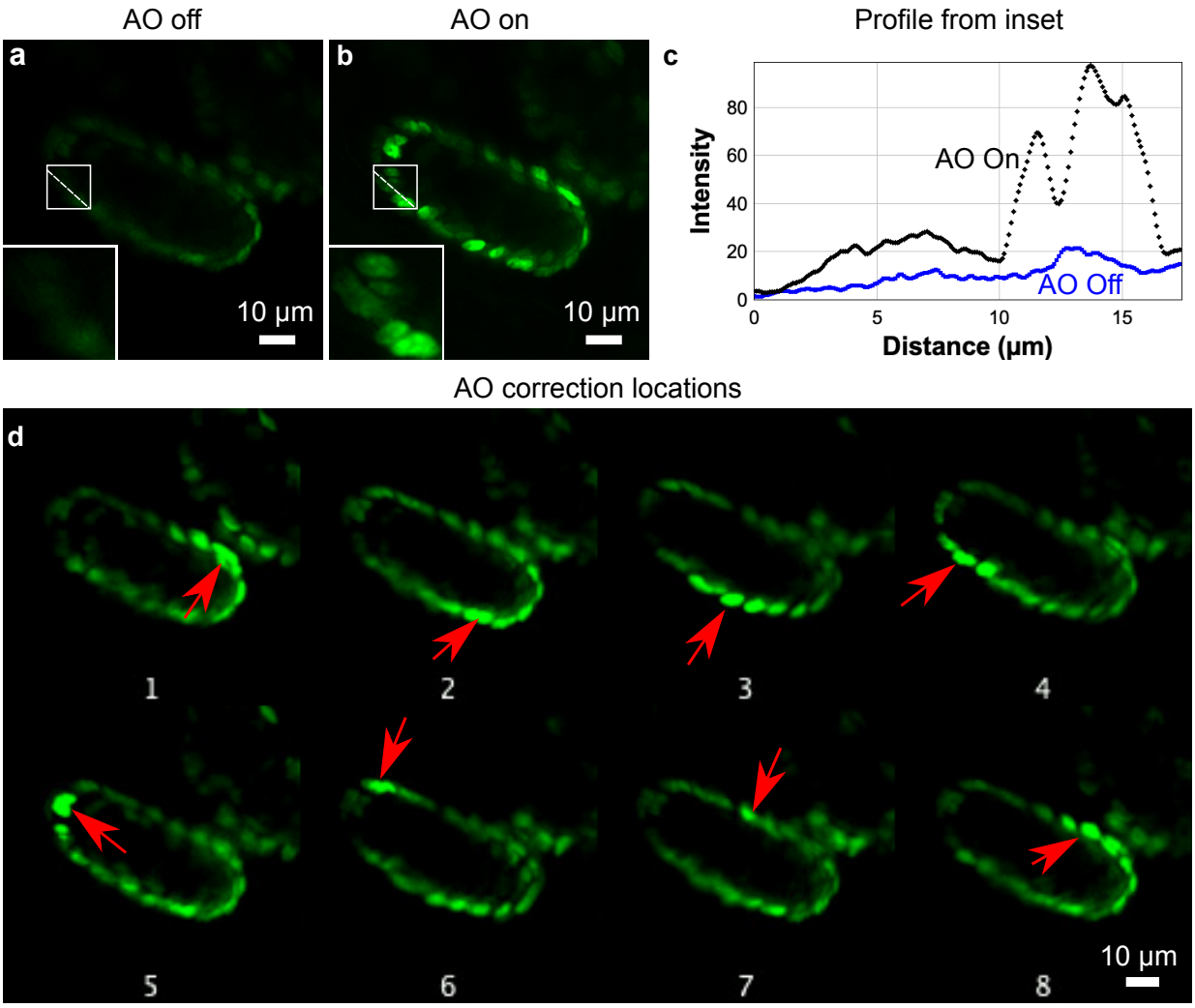

Figure 1.3: GFP tagged keratinocytes in murine skin, images acquired 400 µm deep into the skin through the fat side of the skin. **a.** The image acquired with a system correction (flat wavefront), but no sample aberration correction. **b.** The complete AO corrected image, which uses eight different single point corrections, centered on individual keratinocytes. The image displayed here is a maximum intensity projection of the 8 different corrected images. **c.** Plot of the fluorescence intensity diagonally across the insets in panels a and b. **d.** The eight locally corrected images that contribute to panel b are shown, with red arrows pointing out the cell used as the optimization guide star. The colormaps used in the images have the same minimum (0) and maximum (100) in panel a and b, and the same minimum (0) and maximum (80) in panel d across all 8 of the constituent images.

1.3.4 Volumetric corrections in aberration inducing samples

To quantify the performance of the interpolated volumetric wavefront correction system, samples were prepared with different concentrations of 10 µm diameter glass beads for optical scattering, and 1 µm (sub-diffraction) yellow-green fluorescent beads evenly distributed throughout the sample. Wavefront corrections are performed at evenly spaced intervals in depth to produce a network of AO corrections (Fig. 1.4a). A complete z-stack is acquired with the interpolated wavefronts, as well as with the adaptive optics off measurements, which only uses a system correction – i.e., a flat wavefront in the back focal plane, optimized at the top surface of the sample. In the minimally scattering sample, Fig. 1.4c, the Rayleigh length (a.k.a. depth of field or Z - resolution) stays approximately the same as a function of depth after the AO corrections denoted by the green star at 50 µm depth. The bead brightness also decreases slowly (Fig. 1.4d). In Fig. 1.4e-g, the scatterer concentration is approximately 500,000 glass spheres per mL. Without adaptive optics, the Rayleigh length increases rapidly from a diffraction-limited 4.3 µm to around 8 µm. In contrast, the wavefront corrected beads maintain a Rayleigh length of roughly 4.3 µm throughout the entire volume. Fig. 1.4h-j demonstrates the limitations of the AO correction network. The number of AO corrections is higher than in the lower concentration samples; however, between 400-800 µm, the correction was performed underneath an air bubble in the sample. As a result, the interpolated wavefronts are only valid for beads close to the guide stars, giving a region with low intensity distorted beads so that Gaussian-Lorentzian fitting did not converge – hence the gap in the data in Fig. 1.4i. However, after 800 µm depth, the AO system recovers nearly diffraction-limited resolution. Overall, as long as the spacing between guide stars is correctly chosen, the 3D-AO system maintains nearly diffraction-limited resolution throughout the samples, whereas the flat wavefront images rapidly lose resolution due to optical scattering.

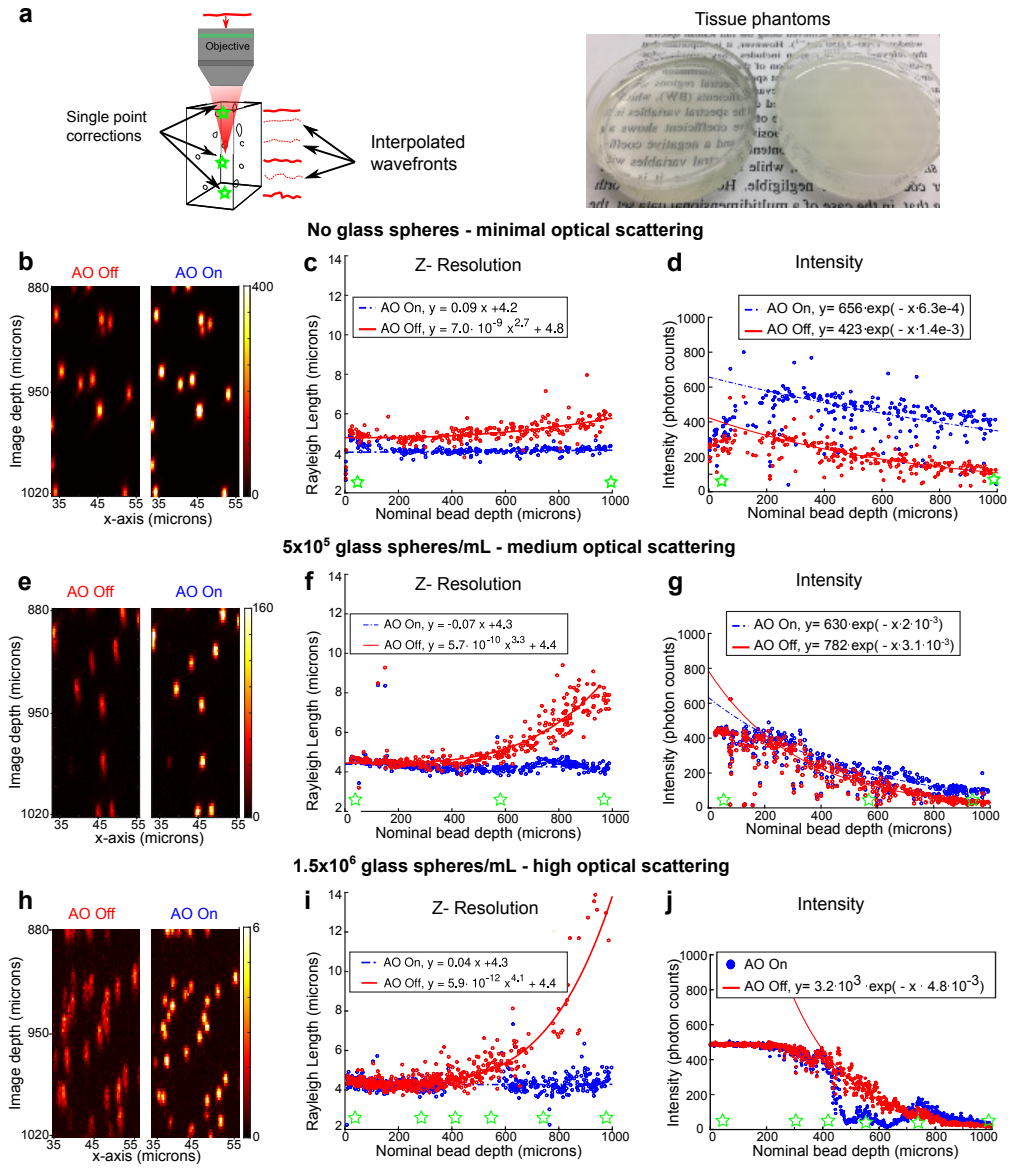

Figure 1.4: **a.** Validation of the 3-D AO network technique using sub-diffraction fluorescent beads in tissue phantoms imaged with a 20x 0.4 NA air objective and 780 nm excitation light. **b., e., h.** X-Z cross sections showing the fluorescent beads 0.9 mm deep in the clear tissue phantom with AO corrections (indicated by the green stars) interpolated between the top of the sample and at 1 mm depth. **c.** In the minimally scattering sample, the Rayleigh length (Z-resolution) stays approximately the same as a function of depth for both AO corrected and uncorrected samples. Equations in the plot legend represent the best fit equations, with a linear fit for AO on resolution, and a power law for AO off resolution. **d., g., j.**, Bead brightness decays approximately exponentially with depth for both AO off and AO on images. Plot legend shows best fit exponential expressions. For all plots the laser power is kept constant throughout the entire sample, resulting in detector saturation (flattening of the intensity vs bead depth) over the first 200 microns in **g** and the first 400microns in **j**. In the scattering samples **f., i.**, without AO correction, the Rayleigh length rapidly increases according to a power law, with an exponent related to the concentration of scatterers. With AO corrections the Rayleigh length stays almost flat, shown with a linear best fit line. The increased scattering requires more AO corrections to keep the resolution diffraction-limited.

1.3.5 THY1-YFP transgenic mouse brain

A THY1-YFP mouse brain was purchased from Jackson labs (Bar Harbor, ME) to compare the AO DIVER to conventional epi-detected imaging performance. Motor neurons in the brain express yellow fluorescent protein (YFP), illuminating the cells throughout the tissue. The image in Fig. 1.5a is acquired in a single pass (without tiling) with a 4X 0.1 NA air objective. The wide area of the DIVER detector (18×18 mm) enables a 15 mm wide field of view without vignetting.

The epi-detected images (panels 1.6 a, e, i, m) are compared to the DIVER detected images, both with only a system aberration correction(panels 1.6 b, f, j, n) using a 20X 0.4NA air objective. Images from the DIVER are also shown with local adaptive optics corrections(panels 1.6 c, g, k, o). The entire volume is then imaged with the complete 3D AO network. Intensity profiles (panels 1.6 d, h, l, p) represent the fluorescence photon counts across the image in the x-direction, centered over the central neuron in the images. Intensity for each plot is averaged along 15 µm in the y-direction in the image. After a millimeter depth, the epi detector is unable to resolve details such as the axons or dendrites, whereas the DIVER channel clearly resolves neurons nearly 2 millimeters into the sample. Signal to noise ratios calculated from panels 1.6 d, h, l, p are improved from epi - AO off to DIVER - AO on by a factor of 6, 5.6, 3, and 2 respectively. The decreasing size of the isoplanatic patch as a function of depth is evident when comparing the AO On DIVER images, improving in the brightness of the central neuron, with a radially decreasing image brightness. A side view of the tissue (X-Z maximum intensity projection) shown on the right of Fig. 1.6, compares the AO off epi-detected image (panel 1.6q) to the AO on DIVER detected image (panel r) both imaged to a maximum depth of 2.1 mm.

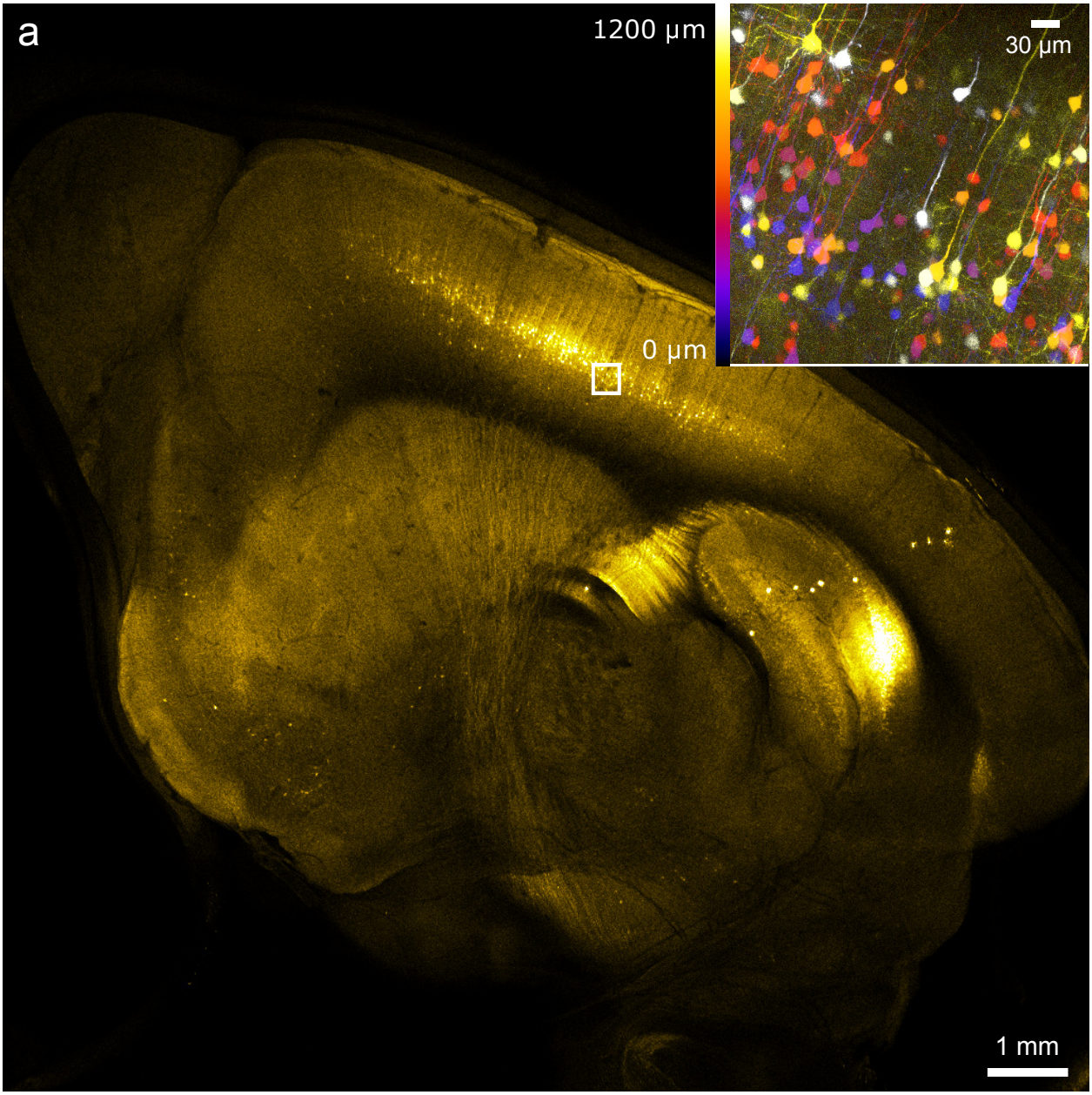

Figure 1.5: **a.** Thy1-YFP transgenic mouse brain, imaged with a 4x0.1NA air objective with a field of view of approximately 14 mm. Motor neurons strongly express yellow fluorescent protein (YFP), providing the contrast in the image. The region of interest in the inset is a maximum intensity projection (z) of the data shown in Fig. 1.6 panel r, acquired with adaptive optics and a 20x0.4NA air objective, pseudo-colored according to the depth (AFP- actual focal position) of the imaging plane- from the first 1.2 mm below the top surface of the tissue slice. Scale bar = 1 mm.

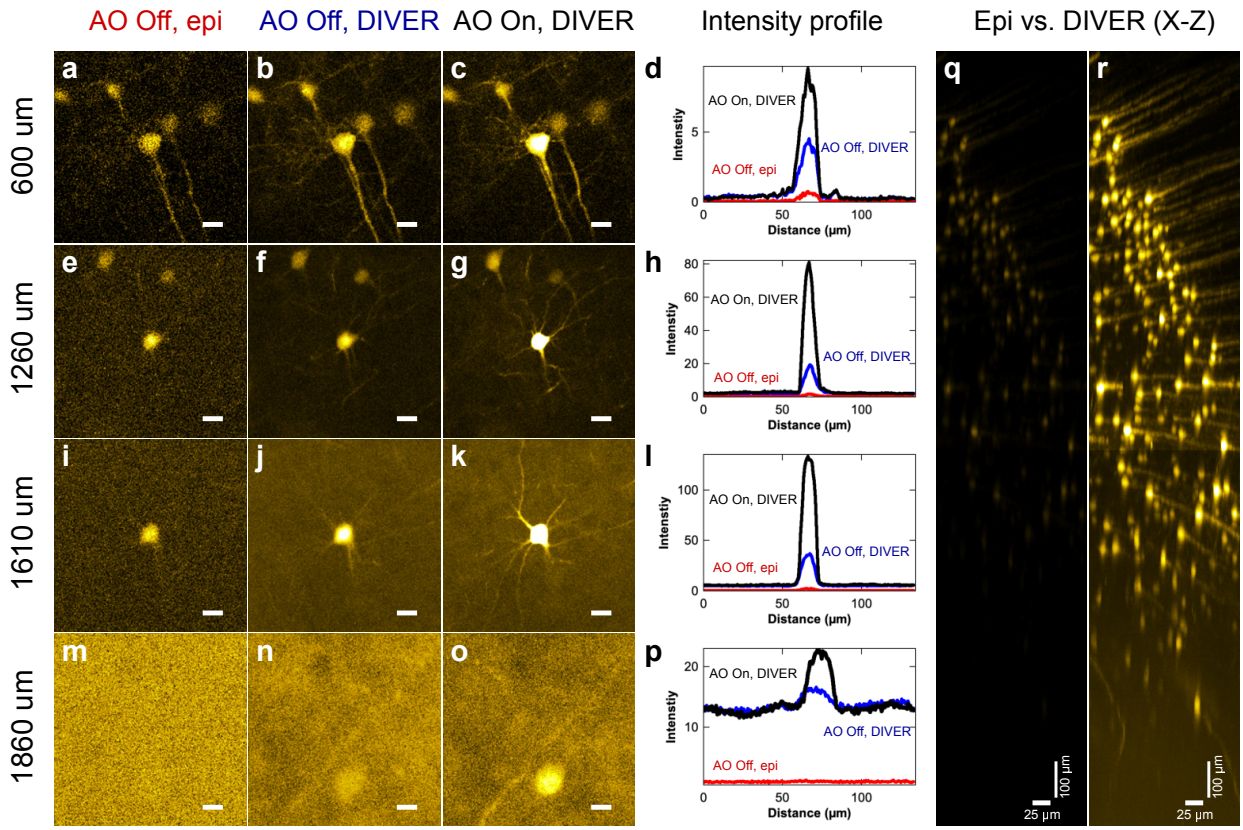

Figure 1.6: Two-millimeter deep Thy1-YFP brain imaging with two-photon excitation (950 nm) of YFP (yellow fluorescent protein) tagged motor neurons. Image depths are indicated on the left of the figure. Epi-detection channel (**a, e, i, m**) and the DIVER detection channel (**b, f, j, n**) without sample correction. After AO optimization, the images in panels (c, g, k, o) are acquired. In panels (**d, h, l, p**), the surface profile across the central neuron shows the difference between adaptive optics on and the system correction (AO off) is about a factor of two in the DIVER channel. In all images in the ***AO off, epi-detector*** column, pseudocoloring is adjusted to maximize the contrast in the image due to the small signal range. In the ***AO off, DIVER*** and ***AO on, DIVER*** columns, the same minimum (0) and the maximum value is used to pseudocolor the corresponding images. The maximum value is selected to saturate no more than 10% of pixels in the AO on image. **q.** A side view of the YFP brain with AO off, acquired using the conventional epi-detector. **r.** Side view with AO on, using the DIVER detector, both images use the same colormap range. All scale bars = 25 μm unless indicated.

1.4 Discussion

The ability to resolve subcellular structures millimeters deep into tissue will accelerate clinical and scientific discoveries. By noninvasively imaging cells in their native environments with submicron resolution, we can leverage the broad range of existing light-based biosensors and endogenous fluorophores to understand signaling, morphogenesis, and protein expression and dynamics in complex systems. Improved signal detection and control over light propagation in space and time are paramount to achieve millimeter-scale imaging in biological samples. We implemented AO technology in combination with the DIVER detector to push the limits of deep-tissue imaging using skin and brain tissue as example applications.

Our AO method uses a single point intensity approach over image-based wave front sensing [25, 18], resulting in a speedy optimization that does not require spatial coherence. Regardless of image quality, the algorithm improves the focusing of the excitation light and enhances the image. The system is also relatively insensitive to optical alignment and mirror mode orthogonality, in contrast to conventional indirect and direct wavefront sensing methods [22, 26]. The simple wavefront correction algorithm makes adaptive optics more accessible to microscopy labs and users. Three steps are required to improve the optical resolution throughout a volume of interest: point and click on the guide stars throughout the sample, press a button to start the optimization algorithm, then start imaging.

Conventional MPM produces high-resolution images in thinly-sectioned samples, but it is often necessary to acquire information throughout tissue at different depths. Wavefront corrections can be extended to three-dimensions using wavefront interpolation (Fig 1.4a). Interpolation allows faster wavefront correction, but the density of corrections increases for more heterogeneous samples and with the imaging depth. The correction density depends strongly on the sample, so we used a trial and error approach to improve the image with the lowest number of corrections. The AO DIVER resolved neuron subcellular structure up to approximately 2mm deep into the mouse

brain, with an increase in the signal to noise ratio by a factor of more than 5 when compared to conventional approaches. Deep imaging, possible with the AO DIVER, can be used to study the pathogenesis of neurological disorders such as Parkinson's Disease [27].

Although laser scanning microscopy is relatively slow, AO DIVER technology can be combined with other imaging modalities, for example, using a single plane illumination technique [28]. An extension of our AO system to SPIM will facilitate rapid imaging and could be applied to imaging neuronal activity.

In summary, we have identified and addressed the critical considerations in the development of a 3D AO corrected deep tissue microscope. The AO DIVER brings together advanced light shaping technology and efficient signal detection to extend the fundamental limits of deep tissue imaging and make deep tissue imaging accessible and robust. By improving light focusing into the sample and making use of stray excitation light, fluorescence signal generation is more efficient and allows lower laser powers to be used – reducing phototoxicity and sample damage – enabling more physiologically accurate measurements.

1.5 Methods

1.5.1 DIVER Microscope

Details of the DIVER detector construction can be found in [9]. The detector is a photomultiplier tube (PMT) (Hamamatsu R7600P-300) with 18×18mm photocathode area. The PMT is optically coupled to a filters/shutter and filled using an index matching liquid (propylene glycol). Two BG39 filters (Schott) of 25mm diameter are used as windows to seal the chamber and block the excitation laser light.

1.5.2 Single point AO optimization

We use a deformable mirror with 37 hexagonal segments (Boston Micromachines Corp.). Each rigid mirror segment has three actuators which allow full tip – tilt – piston (X tilt, Y tilt, Z-depth) control of each segment. In total the imaging system has 3x37 = 111 degrees of freedom. To effectively map out the energy landscape, the Simplex algorithm is initialized with $n+1$ mirror shapes that approximate the Zernike polynomials. Zernike polynomials are often used to constrain the search space in indirect wavefront sensing methods [26].

The feedback loop is shown in Fig. 1.1a. A femtosecond (fs) laser illuminates the deformable mirror (DM). The DM produces a phase shift, ϕ_{DM}, which is optically conjugated using a 4-F lens system to the X-Y scanners. The scanners are optically conjugate to the back focal plane of the microscope objective. Upon propagation through the sample, heterogeneities in the refractive index throughout the sample cause phase aberrations, which decrease the excitation intensity. Fluorescence light passes from the focal point through a series of absorptive bandpass filters. The signal from the wide-area detector is then digitized and averaged. The algorithm generates the next DM setting and optimization continues until the fluorescence intensity stops increasing.

The segmented DM has a frame rate of about 40kHz (25 µs), so that the rate limiting step in the optimization loop is the fluorescence light collection. In the absence of other noise, the confidence that a DM setting ϕ_i improves light focusing scales with the square root of the product of the irradiance value λ_i and the time over which the photons are detected T,

$$\mathrm{SNR}_i \simeq \sqrt{\lambda_i T} \tag{1.5}$$

The best strategy for 2PEF optimization in the AO DIVER is to keep the laser power low to minimize photobleaching, but high enough to maintain an average photon count of at least 0.1 photons/microsecond. With an acquisition time of 15 ms per setting ϕ_i, this gives a signal to noise ratio

of about 38. For small perturbations to the wavefront, the optimization routine typically converges after 800 iterations. The routine is run 3 times with added noise each time, to ensure that the algorithm is not stuck in a local minimum. For a typical optimization sequence of 2400 iterations, there are about 3100 total function evaluations on average, which for dim samples takes $\simeq$45 seconds. For very bright samples, the irradiance can be much higher, allowing a shorter acquisition time of about 5 ms, giving an optimization time of $\simeq$15 s. We also characterized different AO optimization approaches by simulation – see Methods 1.5.8. The simulation indicated that optimizing all segments simultaneously was less likely to get stuck in local minima than optimizing one segment at a time. Simultaneous optimization also worked faster than optimizing mirror segments individually or in groups, because of time saved in the initialization steps and in the termination criteria. These results were confirmed experimentally (data not shown).

1.5.3 3D AO corrections

To image large 3D samples with AO we developed a user interface in SimFCS (www.lfd.uci.edu) to help guide the correction process. The focal point is first centered on a local bright spot by the user clicking on the image, which parks the scanner at the desired location. We record the absolute x, y, z position relative to the center of the top of the imaging volume, then optimize to find the best wavefront correction that maximizes the brightness and minimizes the excitation volume. Then the stage is moved to the next z-position, and the next wavefront correction is obtained. If this is done with fine enough z-spacing, we can linearly interpolate the wavefront for arbitrary points between single point corrections, as demonstrated in Fig. 1.4. The maximum z-step size between corrections depends on the scatterer size, distribution, as well as the numerical aperture of the objective, and the depth of the imaging plane. Using the flat field of beads, we characterized shifts in the field of view caused by optimization in the vicinity of brighter local objects. The possibility to sense brighter objects and shift the field of view depends on the effective focal length of the objective being used (see Supplemental Fig. 1.8), but typically the buffer region from a brighter

object should be greater than 1-2 µm when using a 40x 0.8 NA water objective, and about 3 µm when using a 20x 0.4NA air objective. In other words, if there is a brighter object within one-two axial PSF lengths, the AO system can sense and move towards the brighter region.

1.5.4 Quantifying optical resolution

The sub-diffraction size of the beads allows us to fit the beads to a 3-D Gaussian-Lorentzian, a model of the two photon excitation point spread function [29],

$$I(r,z) = \frac{2I_0 w_0^2}{\pi w^2(z)} \exp\left(-\frac{2r^2}{w^2(z)}\right) \tag{1.6}$$

with

$$w^2(z) = w_0^2\left(1+\left(\frac{z}{z_R}\right)^2\right). \tag{1.7}$$

The volumetric data are first binarized by $3\times3\times3$ median filtering and intensity thresholding. Bead centroids and bounding box are found using Matlab's bwconncomp and regionprops3 functions. The results from the regionprops3 function serve as the initial guesses for the volume fitting, and a least-squares minimization is then performed (using Matlab's fmincon) to find the optimal parameters, I_0, w_0, and w_z to fit the original unprocessed data. The exponential fits used in Fig 1.4d,g,j give an estimate of the wavefront aberration. For small deformations in the wavefront, the Maréchal approximation [30, 31] gives the result that the intensity of an aberrated focus relative to the intensity of an unaberrated focus, is related to the RMS phase variation, $\Delta\phi$,

$$I_{ex} \sim I_0 e^{-(2\pi\Delta\phi)^2}. \tag{1.8}$$

1.5.5 Tissue Phantoms

1 micron diameter YG fluorescent microspheres (Polysciences inc., Warrington, PA) are dispersed into P4 clear silicone using a Vibracell sonicator (Sonics & Materials inc, Newtown, CT). After dispersing the microspheres, we added the 9-13 μm glass spheres in various quantities to induce a blurring effect in the sample. Images are acquired with a 20X 0.4 NA air objective, 780 nm excitation light, and a 400-600 nm bandpass filter for emission light.

1.5.6 Tissue Samples: K14-GFP skin

Fresh mouse skin was resected from the back of a K-14 GFP transgenic mouse. The sample was mounted in 1x phosphate buffered saline on a microscope slide, and covered with #1.5 cover slip. The sample was imaged within 5 hours of resection through the fat side of the skin. The images in Fig. 1.3 are obtained with a 20x 0.4 NA air objective with 900nm excitation, and 575±75 nm bandpass filters for emission light.

1.5.7 Tissue Samples: Thy1-YFP brain

A Thy1-YFP H. Jrs. (yellow fluorescent protein-tagged motor neurons) mouse brain, fixed in 10% neutral buffered formalin, was purchased from Jackson Labs (Bar Harbor, ME). The brain was sectioned sagittally with a razor blade to a 2-millimeter thick slice. The slice was placed between a microscope slide and a #1.5 coverslip with agarose to stabilize the tissue and coverslip. After initial attempts to image the ROI shown in Fig. 1.5 tissue with adaptive optics, it was determined that residual formalin in the tissue was causing the YFP to photobleach too quickly to optimize the image. The tissue slice was washed for 3 hours in a 4°C solution of phosphate-buffered saline, 5% glycerol, and n-propyl gallate, an antifade compound from Sigma Aldrich (St. Louis, MO), to decrease the bleaching effect.

The image in Fig. 1.5a is acquired in a single pass (without tiling) using two-photon excitation of YFP with 950 nm light with a 4X 0.1 NA air objective, and an emission bandpass filter of 575 nm ±75 nm. The wide acceptance angle of the DIVER enables a 14 mm wide field of view without vignetting. In Fig. 1.6, images are acquired using two-photon excitation of YFP with 950 nm light with a 20x 0.4 NA air objective, and an emission bandpass filter of 575 nm ±75 nm. The excitation laser power is increased exponentially as a function of depth to compensate losses to absorption and scattering in the sample.

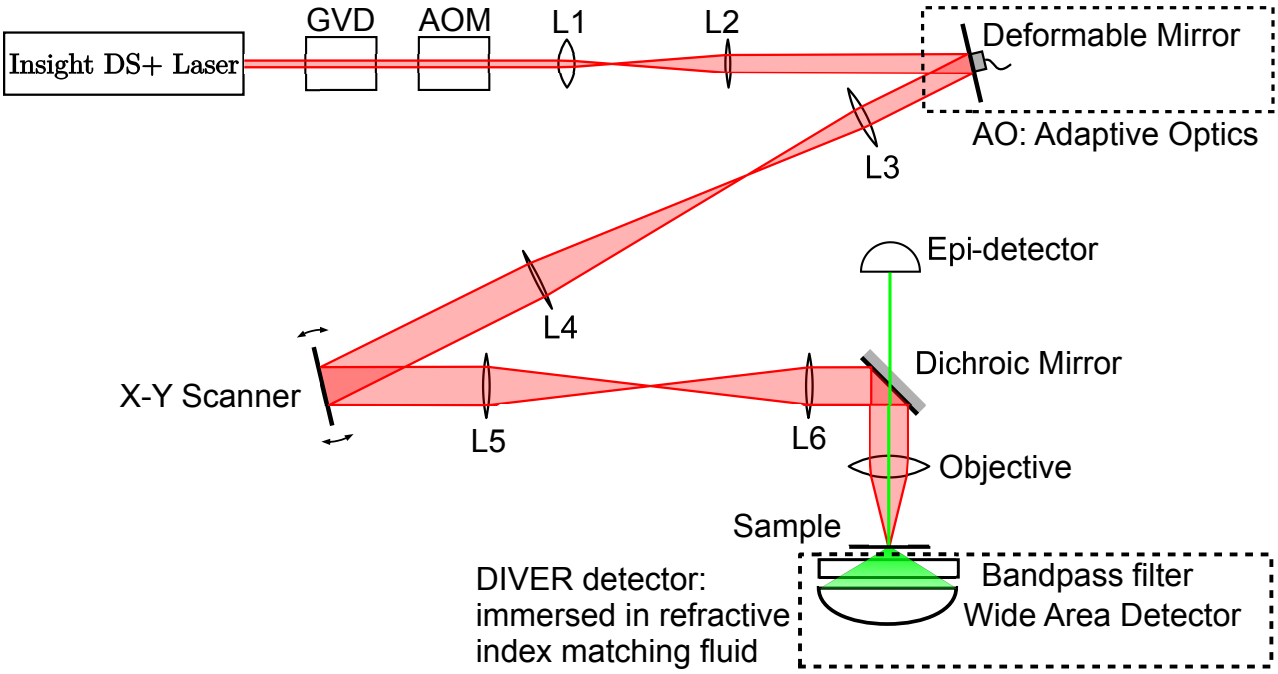

Figure 1.7: The AO DIVER multiphoton microscope. We use an Insight DS+ laser with a Deep See attachment (GVD) to compress the pulse and correct for group velocity dispersion in the optics and the sample. Laser power is attenuated with an acousto-optic modulator (AOM), then the laser is expanded to fill the aperture of the Boston Micromachines Hex-111 Deformable Mirror (DM). The DM is conjugated to an X-Y galvo scanner using a beam expanding lens system. The Galvo scanner is then conjugated to the back focal plane of the objective. Some of the fluorescence light is collected by the objective lens, then passes through a dichroic mirror and bandpass filter to the conventional epi-PMT, a Hamamatsu photomultiplier detector. Fluorescence is also collected by the DIVER detector. Excitation light is filtered out using two BG-39 absorptive filters, and a filter wheel containing a bandpass filter is used to select wavelengths of interest. The entire DIVER assembly is filled with refractive index matching liquid to maximize light coupling from the sample into the wide area Hamamatsu photo multiplier tube. [1]

1.5.8 Simulations

We developed a simulation of our imaging system to better understand the influence of the DM. The model takes in a user-defined beam profile, typically in the form of a Gaussian beam. We then generate a phase function that defines the aberration of the overall imaging system (sample plus optics). The intensity distribution of the focal volume is then calculated using a Fourier transform of the complex electric field. The maximum value of the focal volume is used to predict the fluorescence signal that serves as the cost function in the optimization algorithm.

AO-enabled image acquisition and optimization software was developed using Delphi. The AO interface was built on top of Globals SimFCS, a program developed in the LFD (Laboratory for Fluorescence Dynamics) for fluorescence microscopy. Data analysis was performed using Matlab and Python.

1.5.9 Depth calculation

The imaging depth, or actual focal position (AFP) is calculated using ray optics and estimating the different indices of refraction in the optical setup. The AFP is calculated from the linear encoder readout on the translation stage,

$$\mathrm{AFP} = \tan(\arcsin(\mathrm{NA}/n_2)) * ((\tan(\arcsin(\mathrm{NA}/n_1)))$$
$$\times(\mathrm{NFP}+c)/(\tan(\arcsin(\mathrm{NA}/n_2))) - c)/(\tan(\arcsin(\mathrm{NA}/n_3)))$$

with NA for numerical aperture, n_1, n_2, n_3 the refractive indices of the objective immersion fluid, coverslip, and sample mounting fluid respectively. c is the thickness of the coverslip in microns.

1.5.10 DM translational modes

The deformable mirror can produce translational modes, known as tip-tilt and defocus. The total translation depends on the effective focal length of the objective used, the total rotational angle of the deformable mirror, and the radius of curvature of the deformable mirror. The translational modes are illustrated below in Fig. 1.8.

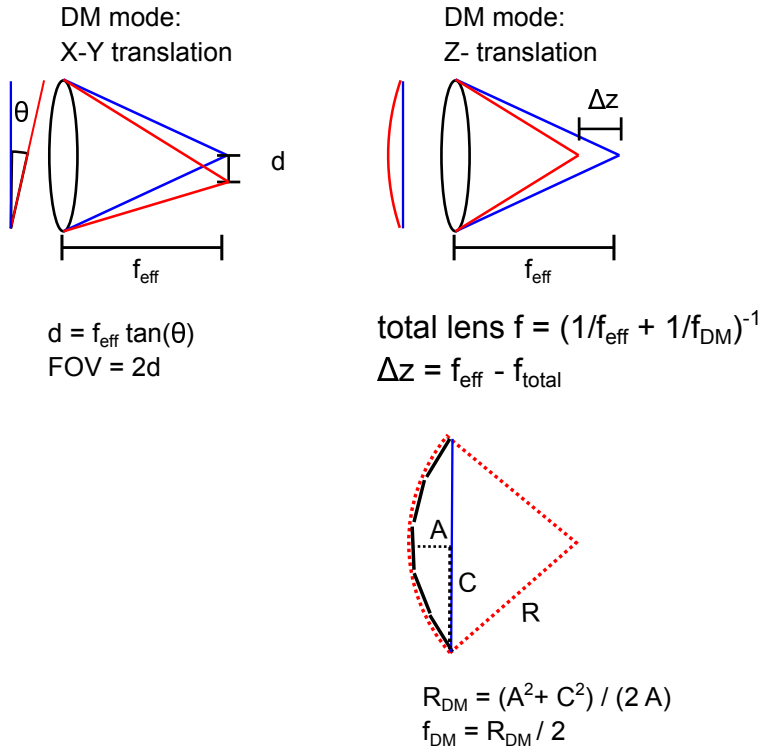

Figure 1.8: Deformable mirror translational modes. The translational potential depends on the microscope objective focal length and deformable mirror deflection properties.

Chapter 2

Ultrafast 3D scanning in the AO DIVER with a segmented deformable mirror

2.1 Abstract

The deformable mirror in the AO DIVER can actively correct image aberrations as well as translate the focal point of the microscope, allowing rapid laser scanning in three dimensions. This opens up a wide range of possible applications, including rapid 3D imaging, high speed orbital tracking of fluorescent objects, and random-access microscopy. The focus of this chapter is the development of a user interface for the MEMS deformable mirror to enable the aforementioned applications. Proof of principle experiments used in characterizing the translational modes in the AO DIVER are presented, calibrating the deformable mirror modes and confirming the theoretical scanning range of the deformable mirror.

2.2 Introduction

Fast scanning is essential for rapid volumetric imaging, enabling *in vivo* measurements of physiological activity with sub-cellular resolution at millisecond time scales [32, 33, 34, 35, 36, 37]. Confocal and multiphoton microscopes are limited in the maximum frame rates due to the serial nature of raster scanning. Laser scanning microscopes use oscillating mirrors to scan the excitation laser beam through the sample and form high-resolution fluorescence images point by point. Conventional scanning microscopes use two scanning mirrors, one for the x-direction and one for the y-direction. Axial scanning (also known as creating a z-stack, or remote focusing) is typically achieved by moving the sample up or down relative to the objective with a translation stage. Piezo mounts can also be used to move the objective up and down, but they are relatively slow due to the large mass of the objective [38]. Furthermore, physical movement of the objective prevents the use of immersion objectives due to the mechanical coupling to the sample, and the range of movement is relatively small [38, 39, 40]. Many forms of electrically tunable lenses have been developed to shift the focal plane of the beam with varied success [41, 42, 43, 37]. The ideal tunable lens should have a response time of microseconds and introduce a minimum of additional aberrations, however most tuneable lenses suffer from astigmatism, spherical and chromatic aberrations, and relatively slow response times on the order of milliseconds [40], in addition to sample induced aberrations. For these reasons we explored the use of a segmented deformable mirror for remote focusing.

Deformable mirrors (DM) are typically coated with a metal, either silver or gold, meaning that they are nearly achromatic. Further, MEMS-based segmented deformable mirrors have the advantage that the micron-sized mirror segments have very small moments of inertia. This allows the shape of the mirror to be modulated at rates of $\simeq 40$ kHz (25 µs/frame), enabling ultrafast scanning in three dimensions, with the added benefit that sample induced image aberrations can also be corrected.

We have developed a process to calibrate the DM scanner and enable aberration-free and scanning. We have also developed a GUI to interface with the DM and facilitate the different modes of

operation - frame scanning, random access scanning, and particle tracking.

2.2.1 Ultra fast scanning with DM translational modes

Ultrafast laser scanning enables probing of the dynamic processes throughout large regions in samples. To scan through the sample, we used a Hex-111 deformable mirror (Boston Micromachines Corp., Cambridge, MA). The Hex-111 can generate approximations to the three fundamental translational modes, known as tip, tilt and defocus. The translational modes are illustrated in Fig. 2.4 as well as Figs. 2.2 and 2.3.

2.2.2 Numerical mirror mode generation

The Zernike polynomials, $Z_n^m(\rho,\theta)$ form an orthogonal basis set on the unit circle. The polynomials describe the phase aberrations that are possible in a circularly symmetric optical system, of which the first few are listed:

$$\begin{aligned} Z_0^0 &= 1 \rightarrow \text{piston} \\ Z_1^{-1} &= \rho\sin(\theta) \rightarrow \text{y-tilt} \\ Z_1^1 &= \rho\cos(\theta) \rightarrow \text{x-tilt} \\ Z_2^0 &= -1+2\rho^2 \rightarrow \text{(de)focus} \\ &\vdots \\ &\text{etc.} \end{aligned}$$

The Zernike modes Z_1^{-1}, Z_1^1, and Z_2^0 are the translational modes. The x and y tilt modes allow displacement of the focal point in the x-y directions, and the defocus mode allows displacement in the z-direction. A lookup table is used to map the translational modes onto the deformable mirror

and allow the mirror to scan in 3D.

The hexagonal segments of the deformable mirror are rigid, so individually they can create only the piston, tip and tilt modes, shown in Fig. 2.1.

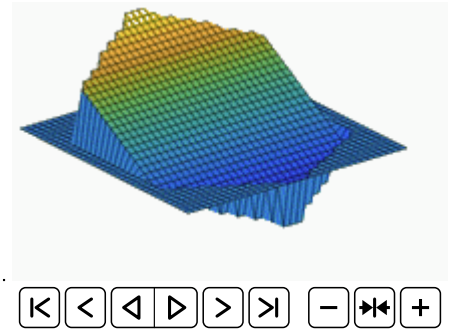

Figure 2.1: Hexagonal mirror segment model. Three actuators per segment means that each segment can move up and down (piston) and tilt in the x and y directions.

The tip (θ_x), tilt (θ_y), and piston (p) of each segment of the deformable mirror can be individually controlled. There are three actuators per segment that can only move up and down, which gives three points in space: $P_0(x_0,y_0), P_1(x_1,y_1), P_2(x_2,y_2)$.

$$\theta_x = 2P_0 - \frac{P_1+P_2}{2P_0} \tag{2.1}$$

$$\theta_y = \frac{P_1-P_3}{P_2} \tag{2.2}$$

$$p = \frac{P_0+P_1+P_2}{3} \tag{2.3}$$

To find the vector of voltages corresponding to the translational mode with all of the mirror segments, an initial guess is made by numerically projecting the phase ϕ onto a matrix of hexagonal segments, $\mathrm{Hex}_i(x,y)$. The average value (or the piston, p_i) of the local phase in the segment is calculated using the formula

$$p_i = a \iint_S \phi(x,y) \cdot \mathrm{Hex}_i(x,y) dxdy \tag{2.4}$$

and the x and y tilts at each segment i are calculated using the formulas

$$\Delta x_i = a \iint_S \mathrm{x} \cdot \phi(x,y) \cdot \mathrm{Hex}_i(x,y) dxdy \tag{2.5}$$

$$\Delta y_i = a \iint_S \mathrm{y} \cdot \phi(x,y) \cdot \mathrm{Hex}_i(x,y) dxdy \tag{2.6}$$

Where a is a factor used to normalize the Zernike integrals over a hexagonal pupil,

$$a = \iint_S \mathrm{Hex}_i(x,y) dxdy \tag{2.7}$$

The mirror model is then reconstructed by summing up all the individual segments (Fig. 2.2, 2.3):

$$\Phi = \sum_{i=1}^{37} p_i \mathrm{Hex}_i + \Delta x_i \mathrm{Hex}_i + \Delta y_i \mathrm{Hex}_i \tag{2.8}$$

The resulting mirror models are shown in Figs. 2.2 and 2.3, as well as a comparison between the point spread function generated by the analytical Zernike modes and the DM approximation.

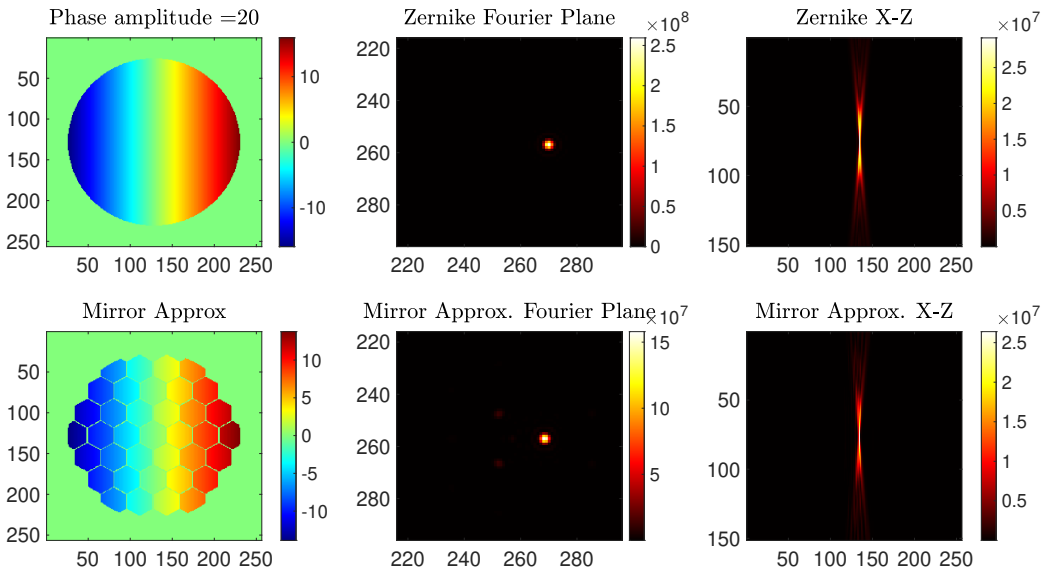

Figure 2.2: Mirror approximation to the Zernike tilt mode (X- translation). In this simulation, a tilt with amplitude of 20 (normalized units) shifts the focal point by 18 pixels from the center at pixel 256.

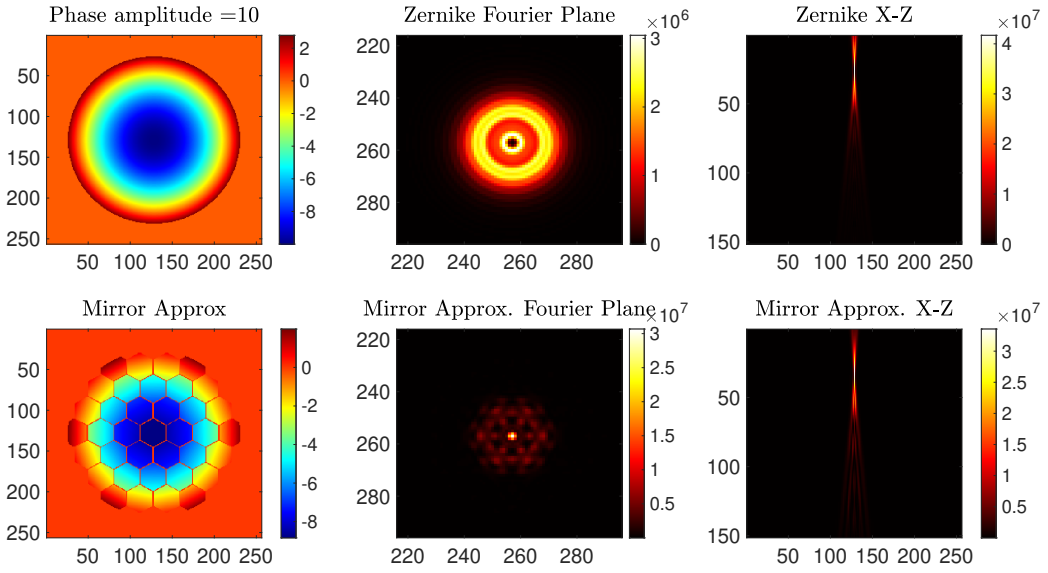

Figure 2.3: Mirror approximation to the Zernike defocus mode (Z- translation).

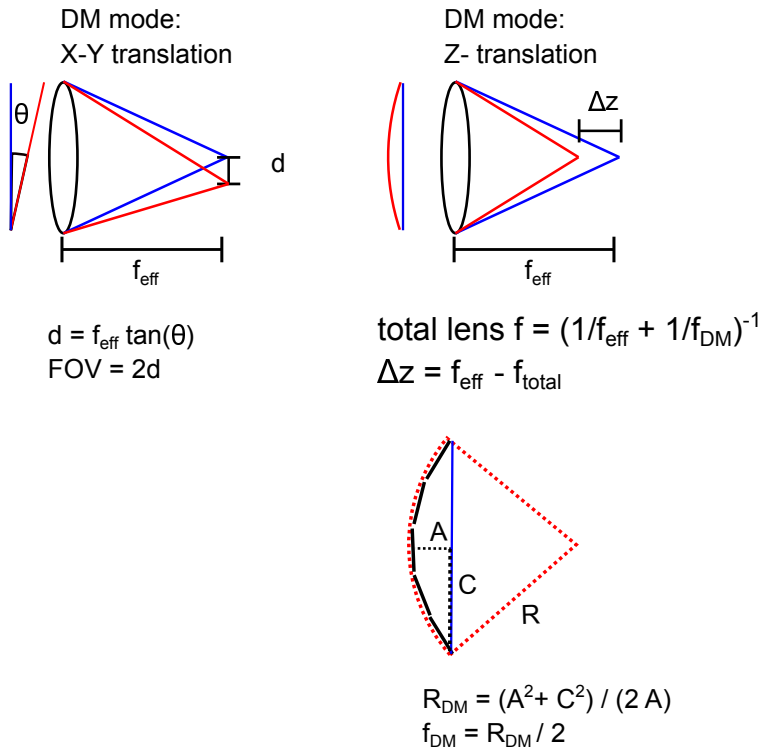

Figure 2.4: Deformable mirror translational modes. The translational potential depends on the microscope objective focal length and deformable mirror deflection properties.

The total lateral translation depends on the effective focal length, f_{eff}, of the objective used, the rotational angle of the mirror, θ_x, θ_y.

$$\text{FOV}_{x,y} = 2 f_{\text{eff}} \tan(\theta_{x,y}) \tag{2.9}$$

Axial translation occurs when the DM takes a concave or convex shape. The distance that the focal point is moved is related to the radius of curvature of the deformable mirror, R_{DM}, and the effective

focal length of the objective,

$$f_{\mathrm{DM}} = \frac{R_{\mathrm{DM}}}{2} \tag{2.10}$$

$$\Delta z = f_{\mathrm{eff}} - \left(\frac{1}{f_{\mathrm{eff}}} + \frac{1}{f_{\mathrm{DM}}} \right)^{-1} \tag{2.11}$$

$$\mathrm{FOV}_z = 2\Delta z \tag{2.12}$$

2.2.3 Feedback loop to generate modes with a segmented hexagonal DM

Two steps are taken to create a lookup table with the translational DM modes. The shape of the surface of the mirror is defined by a vector of 111 voltages that are applied to the piezoelectric actuators of the mirror segments. The vector of voltages is estimated with a numerical model, described in Section 2.2.2. The next step is to calibrate the voltages with a feedback loop that uses the microscope stage to translate the sample, then run a wavefront optimization to allow the mirror to re-center the sample. The process to create a calibrated lookup table is summarized in Fig. 2.5.

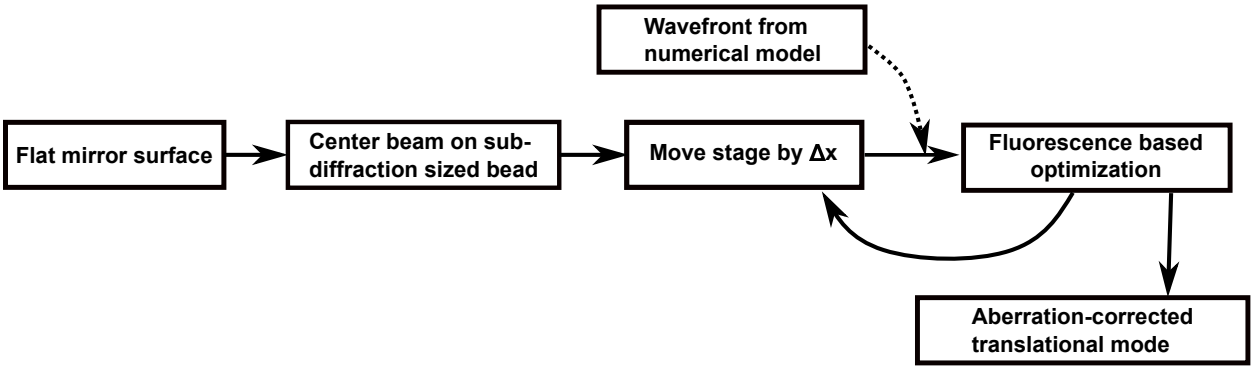

Figure 2.5: Feedback loop for the calibration of translational mirror modes.

2.3 Results

2.3.1 Aberration corrected translational modes

Mirror training

To train the mirror and create an aberration-free lookup table of translational modes, the microscope is first centered on a sub-diffraction (500 nm) yellow-green fluorescent bead. The microscope stage is then shifted by a small amount, Δx, and the deformable mirror is initialized with a numerically calculated vector of voltages. Then the AO optimization algorithm is started (Downhill Simplex algorithm – described in Chapter 1) to find the DM setting that centers the beam on the bead and minimizes the size of the point spread function. After optimization, an image is acquired to assess the validity of the DM setting (Fig. 2.6). Then the stage is shifted by Δx and the process repeats. Finally the vectors corresponding to each translational direction are compiled into a single matrix and orthogonalized using QR decomposition [12]. The resulting orthogonal modes are shown in Fig. 2.7.

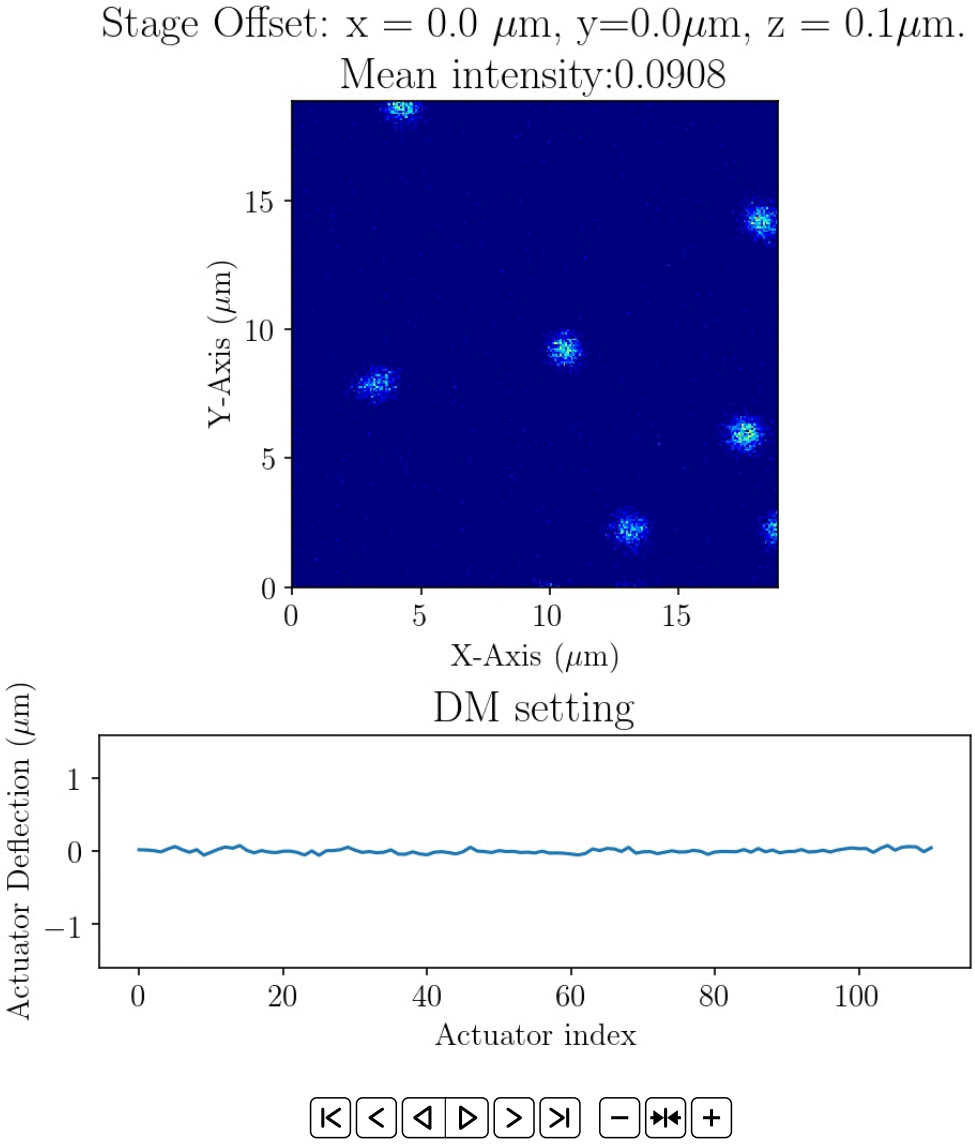

Figure 2.6: The images resulting from the feedback loop in Fig. 2.5. The images in this GIF are acquired after moving the stage by some distance, then re-centering the field of view with the deformable mirror.

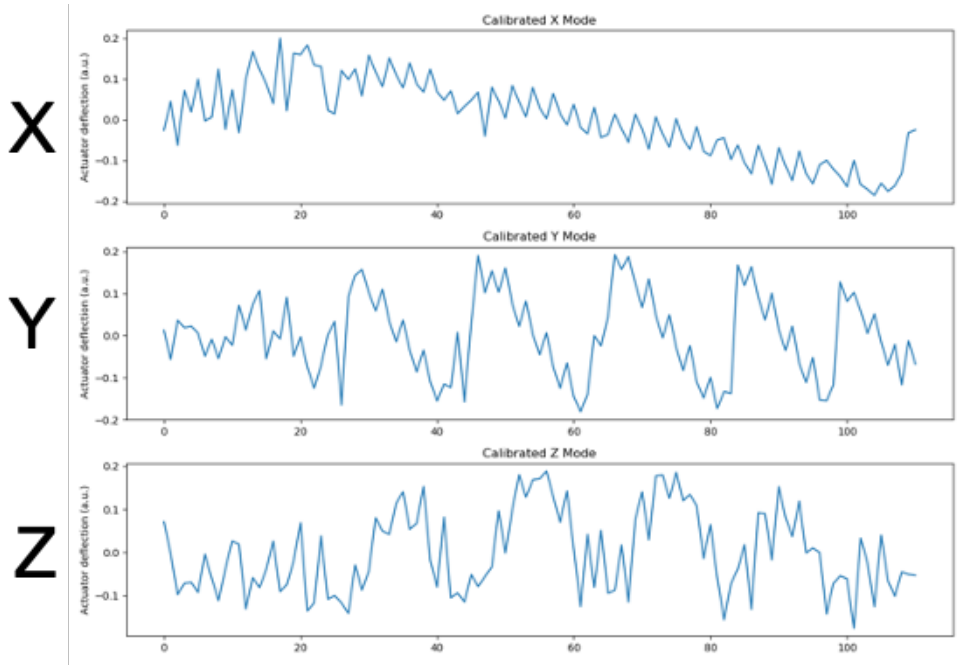

Figure 2.7: The voltage arrays corresponding to the aberration corrected X-tilt, Y-tilt, and Z-defocus modes of the Hex-111 mirror.

Validation of modes

To check the validity of the translational modes acquired from the mirror training routine, a flat field of fluorescent beads is imaged with the addition of different amplitudes of modes to the deformable mirror. The shift in the field of view can then be quantified and validate (or calibrate) the lookup tables.

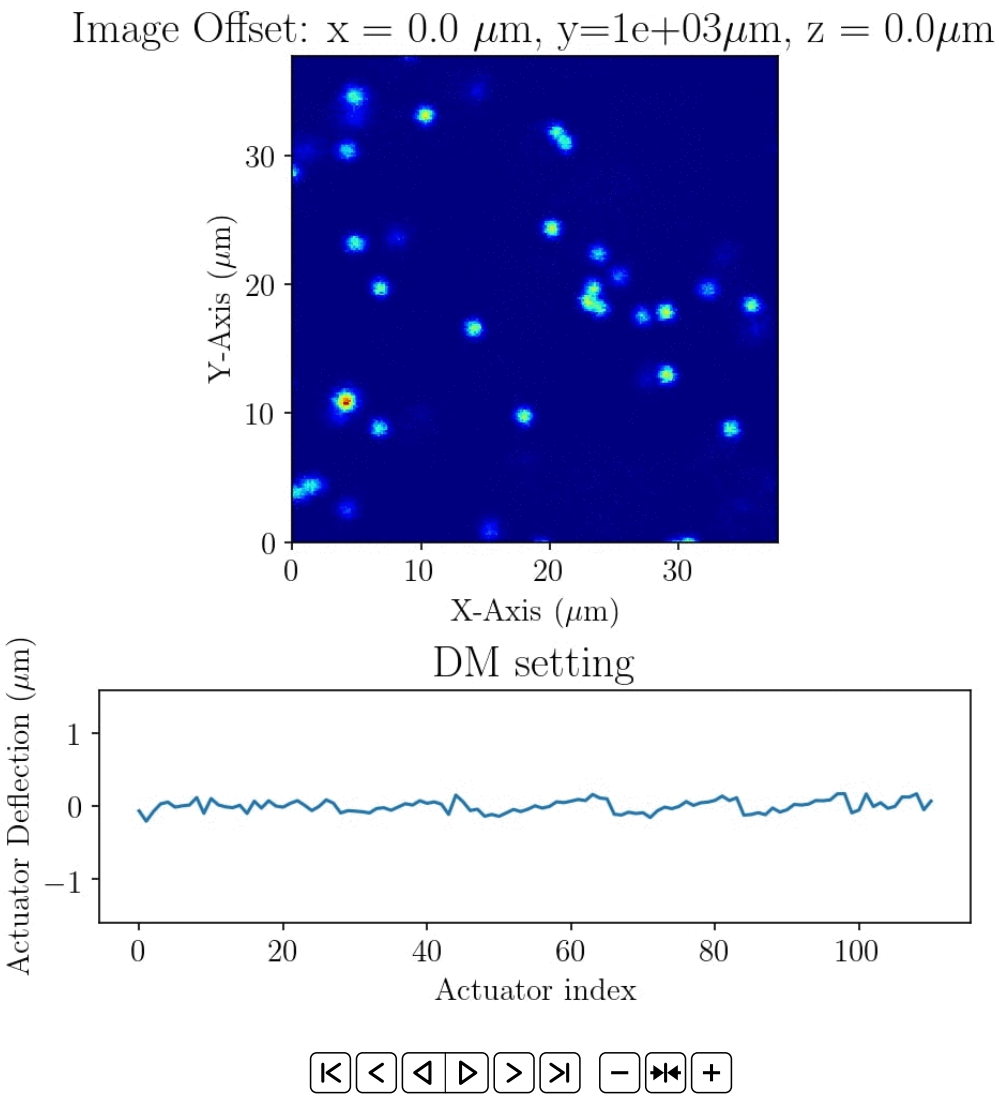

Figure 2.8: Shifting the field of view using the vectors in Fig. 2.7.

2.3.2 DM interfacing

Detection of translational modes during AO optimization

The first application of the characterization of translational modes is implemented in the AO DIVER program described in Chapter 1 to detect the presence of translational modes without the

use of a wavefront sensor. During optimization, the orthonormal translational modes are projected onto the DM state vector and integrated.

To test the technique, the same feedback loop in Fig. 2.5 was used. A random perturbation of Δx, Δy, Δz translated the object with the microscope stage, then the DM was optimized to re-center the field of view. The resulting state vector is then unmixed, and the predicted translation is compared to the microscope stage location (Fig. 2.10).

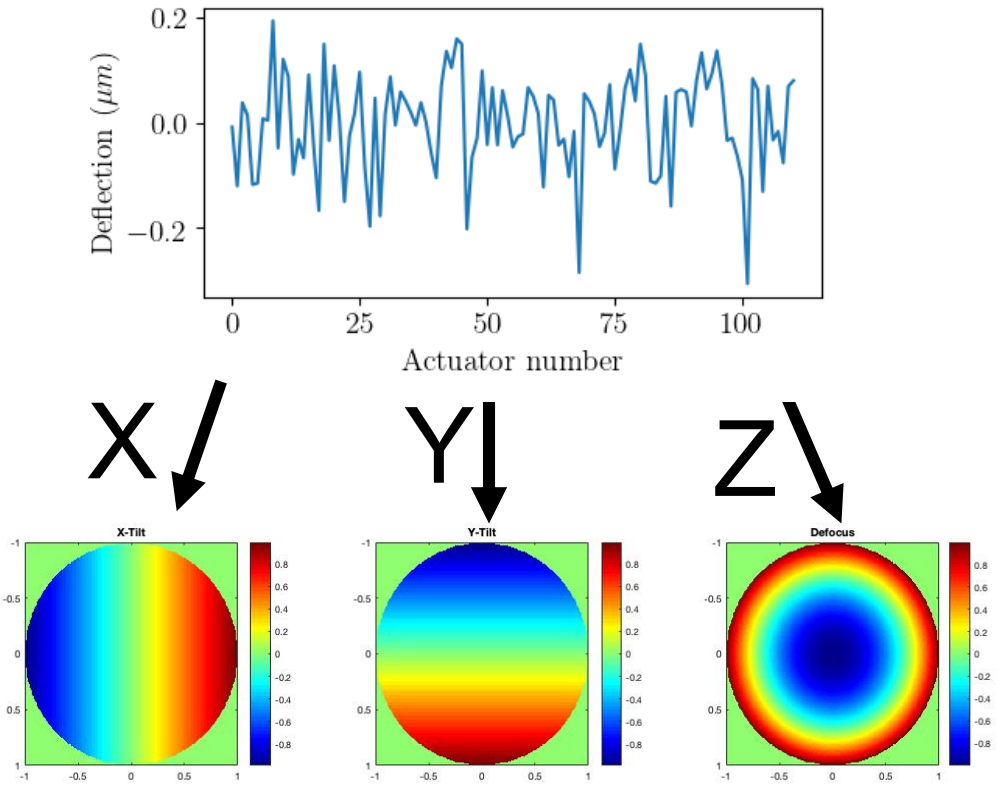

Figure 2.9: The vector of voltages applied to the deformable mirror (the DM "state vector") can be unmixed to detect the presence of tip-tilt-defocus translational modes and minimize the possibility of image distortion during interpolated AO imaging.

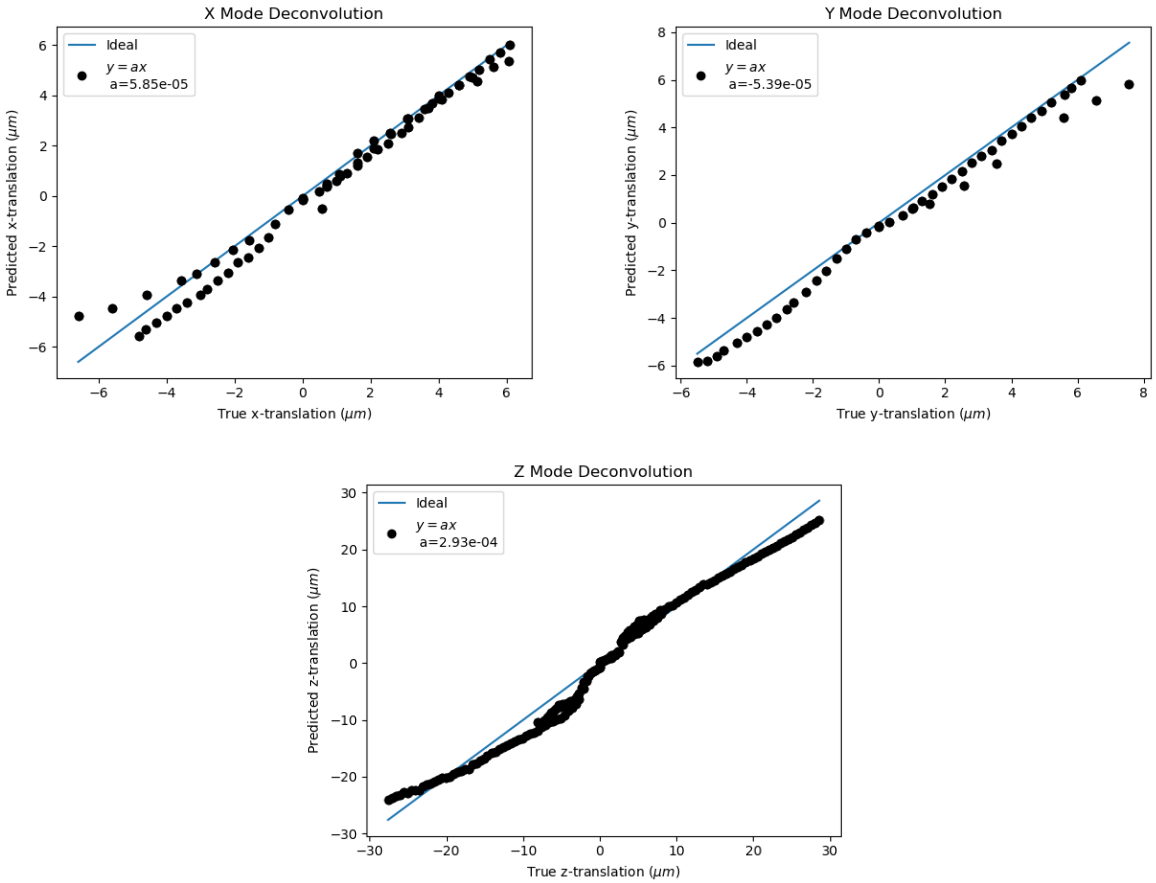

Figure 2.10: Predicted translation using the projection unmixing technique compared to the true microscope stage translation.

Figure 2.11: SimFCS module for deformable mirror based scanning. The module allows frame scanning ("AO scanner") in x-y, x-z, y-z, and x-y-z. The "Scan control points" button allows the selection of any number of locations in the region (shown in graph on the top right), then the DM will cycle through the list of points, parking the beam on each location for some amount of time.

AO scanner: Frame scanning

A graphical user interface (Fig. 2.11) was developed as an add-on to SimFCS to use the DM as a scanner. There are three primary functions in the interface. The first is the scanning feature (top of the GUI in Fig. 2.11) A drop down menu allows selection of the scan type and direction. Pixel dwell time determines the frame rate. The size (FOV) and pixel size of the image is selected with

the x, y and z -pixels fields below the AO scanner button.

Scan control points: Random access scanning

The interface allows the user to select arbitrary points throughout a 3D rendering of the volume of interest (top right graph in Fig. 2.11). A volumetric image is first acquired with the AO scanner button, then the points are initialized by clicking on the rendering. The locations of the points can be controlled by dragging the "x" markers on the graph or more precisely by the x, y, z center fields underneath the control points button.

Synchronized sequencing: DM settings

The DM can be operated as an independent scanning unit, or it can be programmed to operate in a triggered mode, in which the DM driver can be loaded with a sequence that is initiated by an external TTL signal. In this mode the DM is synchronized with the DIVER microscope scanners, enabling the microscope to explore the region around the rigid x-y raster scan at high speeds.

2.4 Discussion

The AO DIVER is a cutting edge deep tissue microscope designed for imaging with high resolution into highly scattering samples. The addition of adaptive optics enables the microscope to image deeper into tissue and creates the possibility to actively scan at high speeds in three dimensions. One potential application is to perform high speed orbital tracking in tissue. Single molecule tracking can be used to follow single biomolecules and monitor the trajectories through cells. The technique can reveal interactions of molecules with their environment, localization dynamics, and transport mechanisms [44, 40]. Another possible application of rapid 3D scanning

with the AO DIVER is to perform random access microscopy [45, 46], a group of techniques that allows sensing of physiological changes in spatially separate parts of the sample. Random access microscopy in conjunction with calcium dyes and GCaMP6 fluorescent proteins [47] have shown promise in neuroscience, allowing researchers to non-invasively measure neurological activity in vivo at kilohertz rates by imaging only the regions of interest, instead of raster scanning over entire volumes [36].

Rapid scanning can also advance image correlation spectroscopy (ICS) methods. Fluorescence correlation spectroscopy (FCS) techniques can detect and quantify the local physical properties of a sample based on fluorescence intensity fluctuations caused by moving molecules, changes in protein conformations, and many other phenomena [48]. Many image-based spectroscopy techniques have been developed with the principles of FCS, probing the dynamic nature of relatively large areas ($\sim$hundreds of microns squared) in biological samples [49, 50, 51, 52]. One image correlation technique – RICS – Raster Image Correlation Spectroscopy [53, 54] relies on that fact that the laser scanned images contain both spatial and temporal information about the fluorophores in a sample. Correlation analysis of the images allows measurement of molecular diffusion processes on time scales of microseconds to seconds. However, existing image correlation spectroscopy (ICS) techniques are limited to 2-D (planar) measurements of the proteins and fluorescent molecules in samples. The addition of a high speed MEMS deformable mirror can be used to expand the technique to three-dimensions and create a better understanding of the diffusion and transport mechanisms in biological samples.

2.5 Conclusion

There are many more applications of the AO DIVER microscope that have yet to be explored. The design of the AO DIVER extends the depth range and field of view possible with fluorescence imaging, and holds promise to extend methods that have only been possible at a single cell level

to a tissue wide scale. The goal of this chapter is to lay the groundwork and develop some of the fundamental tools to enable the range of possibilities.

Chapter 3

Multidimensional imaging and unmixing of Pseudomonas aeruginosa metabolites

Co-authors:

T. Gallagher, A. Dvornikov, K. Perinbam, J. Fong, C. Kim, J. Kapcia, M. Kagawa, A. Grosvirt-Dramen, A. Hochbaum, M. Digman, E. Gratton, A. Siryaporn, K. Whiteson

---

3.1 Abstract

Understanding bacterial physiology in real-world environments is a challenging, yet necessary endeavor to effectively treat infection. The environments of many chronic infections are characterized by steep chemical gradients, yet the effect of hypoxia on opportunistic pathogens can be disregarded in clinical settings. Pseudomonas aeruginosa is a ubiquitous organism that infects wounds and the airways of persons with cystic fibrosis. P. aeruginosa produces pyocyanin, which has been traditionally classified as a toxin due to its redox-active properties, but can also facilitate anaerobic respiration. P. aeruginosa survival in low oxygen is dependent on pyocyanin electron

cycling, but the distribution of pyocyanin metabolism throughout biofilms is not well-understood. To track pyocyanin reduction throughout a biofilm, we developed a fluorescence lifetime imaging microscopy (FLIM) unmixing approach that was compared to hyperspectral imaging microscopy (HIM). Pyocyanin fractional contribution predictions were similar with both approaches. Deep imaging of colony biofilms was performed on a custom-made FLIM instrument designed for tissue imaging, called the DIVER. P. aeruginosa rapidly reduces pyocyanin at the surface of biofilms, where there is dense growth and possibly high oxygen consumption. Our FLIM unmixing approach paired with the DIVER acquisition can be used to track pyocyanin dynamics throughout biofilms and has promise as an application for assessing redox state in relevant chemical gradients.

3.2 Introduction

To persist in any environment, bacteria adapt to chemical and nutrient gradients. Understanding in vivo bacterial metabolism can improve treatment of infections. Chronic lung and wound infections consist of steep oxygen gradients that arise from low penetration and cellular consumption of oxygen [55, 56]. These anaerobic conditions can reduce antibiotic efficacy, especially against organisms inactive in low oxygen [57].

Pseudomonas aeruginosa, an opportunistic pathogen that causes chronic wound and cystic fibrosis lung infections, is incapable of anaerobic growth via fermentation and employs alternative methods to survive in low oxygen. P. aeruginosa can respire anaerobically via denitrification [58, 59] and secrete phenazines [60, 61, 62]. Phenazines are colorful, redox-active molecules that recycle electrons. Pyocyanin, the final product in the phenazine synthesis pathway, has the highest affinity for oxygen out of the phenazine family [63]. In the oxidized form, pyocyanin has a blue pigment and is toxic to other cells [64, 65]. P. aeruginosa uses oxidized pyocyanin to metabolize glucose into acetate, thereby generating more energy and reducing pyocyanin in the process. The reduced form of pyocyanin is fluorescent, but the emission spectrum of pyocyanin overlaps with other

fluorescent metabolites, including NADH and apo-pyoverdine [66].

Hyperspectral imaging microscopy (HIM) can unmix pyocyanin fluorescence from other fluorophores and has been used to study dynamics of reduced pyocyanin in liquid cultures [66]. The spatial production and reduction of pyocyanin has not been characterized, due to limits in the imaging depths of commercial microscopes. The DIVER [10, 67] is a custom-made fluorescence microscope designed for deep tissue imaging that can measure fluorescence lifetimes with single-cell resolution. Fluorescence lifetime imaging microscopy (FLIM) can be used to determine the composition of multiple fluorophores contributing to a fluorescent signal. For example, FLIM is often used to image the relative amounts of enzyme-bound NADH to free NADH, which can indicate the respiratory state of a single cell [68, 69, 70, 71, 72].

FLIM and HIM data can be transformed and represented on phasors, a powerful approach to analyze fluorescence data [73, 74] (Fig. 3.1). For lifetime images, the response of the fluorophore to the excitation source is determined by Fourier transformation of exponential decay traces to obtain the modulation, M, and phase, ϕ, at different harmonics [73]. The sine and cosine coefficients of the transform make up the y and x-axes of the lifetime phasor. Pure species (with single exponential decays) are located on the universal semi-circle (Fig. 3.1A). For hyperspectral data, the modulation and phase are related to the width and mean wavelength of the spectrum (Fig. 3.1B) [74]. Both the fluorescence lifetime and spectral phasor follow the same rule: samples containing a combination of the species fall on a line connecting the sample signal to the pure components. The distance from the signal to the pure component is proportional to the fractional contribution. The phasor is commonly used to unmix two or three fluorescent species using linear algebra (Fig. 3.1), but additional fluorescent species can be unmixed if additional harmonics are incorporated into the phasor analyses. The orthogonality of the Fourier transform guarantees that G and S components for each harmonic can be used as independent observations. This allows unmixing of a fluorescent signal into its constituent components using linear algebra [75] or least-squares optimization if the system is overdetermined. If the bandpass filter used for fluorescence lifetime imaging is the

same as the hyperspectral acquisition window, the fractional contributions to the total signal will be same. This insight allows unmixing of fluorescent species present in each pixel in the image simultaneously using both spectral and lifetime data.

Redox state varies throughout biofilms, and understanding spatial changes in pyocyanin reduction can be used to assess bacterial activity, treatment susceptibility, and infection progression. We developed and compared our FLIM phasor unmixing approach to HIM phasor unmixing. DIVER FLIM acquisition and lifetime phasor unmixing can be used to track pyocyanin redox states throughout P. aeruginosa biofilms.

3.3 Results

3.3.1 HIM and FLIM phasor characterization of P. aeruginosa fluorophores

The two-photon fluorescence emission spectra of P. aeruginosa fluorophores were characterized (NADH, enzyme-bound NADH, FAD, pyoverdine, pyocyanin, 1-hydroxy-phenazine, copoprophoryin) (Fig. 3.2) and agreed overall with previously published spectra [66]. Different reduction methods of pyocyanin changed the fluorescence spectra and lifetime phasor results. The resulting pyocyanin population likely consisted of a mix of the radical and reduced form, but the FLIM phasor analysis suggests the FLIM setup was primarily acquiring the reduced form (Fig. 3.9). Four of the seven species were captured by the FLIM DIVER acquisition parameters, which included an emission filter targeted towards NADH (400-500 nm): NADH, enzyme-bound NADH, and reduced pyocyanin, and apo-pyoverdine (Fig. 3.2). The FLIM and HIM phasor components for the pure fluorescent species were determined (Fig. 3.3). To compare the detected fluorescent species across both methods, the HIM spectral window was truncated to 410-500 nm to exclude measurements of species not captured with our FLIM acquisition settings (Fig. 3.2).

3.3.2 Comparison of HIM and FLIM unmixing results

The spectral and fluorescence fractional contributions of NADH, enzyme-bound NADH, reduced pyocyanin, and apo-pyoverdine were determined at the surface of five-day old biofilms of WT P. aeruginosa PA14 and a phenazine knockout of the same strain (Δphz), which does not synthesize any phenazines including pyocyanin (Fig. 3.4). To assess the robustness of the unmixing approaches across different systems, the P. aeruginosa strains were grown in two conditions, M9 succinate and artificial sputum medium. After imaging the aerobic cultures, the cultures were placed in an oxygen-limited environment for 2h, because we hypothesized that low oxygen would result in reduction of pyocyanin. WT P. aeruginosa PA14 shifted towards the reduced pyocyanin FLIM and HIM signal in hypoxic conditions, and this pyocyanin shift was not observed in the phenazine mutant cultures Fig. 3.5. The FLIM and HIM phasor visualizations indicate pyocyanin contributed to a higher proportion of the fluorescent signal in ASM over M9 succinate media. The HIM and FLIM data were unmixed to determine the fractional contribution of reduced pyocyanin, apo pyoverdine, NADH, and enzyme-bound NADH. The fluorescence lifetime of enzyme-bound NADH depends on local factors, including enzyme type and pH [76], and is not well-characterized in bacterial systems. The FLIM NADH phasor trajectory of P. aeruginosa cultures shifts in different media backgrounds and suggested NADH bound to certain enzymes may have a lifetime shorter than 3.4 ns (Fig. S3.5). We used 2.8 ns as the fluorescence lifetime representation for enzyme-bound NADH in P. aeruginosa. Although Δ phz does not produce pyocyanin, both the FLIM and HIM unmixing methods still detected low fractional contributions from pyocyanin (Fig. 3.6. Overall, HIM and FLIM unmixing did not correlate for the M9 succinate cultures and weakly correlated for ASM cultures Fig. 3.6. Pyoverdine and enzyme-bound NADH have similar spectra and lifetimes, with the narrow spectral band of acquisition, our unmixing method could not accurately distinguish these two fluorophores (Fig. 3.3, 3.2). The HIM and FLIM fractional contributions predictions of pyocyanin were similar in cultures with high pyocyanin production (WT PA14 in ASM) Fig. 3.6B.

3.3.3 Fluorescence lifetime and pyocyanin measurements throughout P. aeruginosa biofilms with the DIVER microscope

The fluorescence intensity and lifetime were acquired throughout different depths of five-day old P. aeruginosa biofilms grown in artificial sputum medium using the DIVER [10, 67]. Laser power was increased with deeper imaging in the sample to compensate for signal attenuation from scattering and absorption. The measured total fluorescence intensity was similar throughout the biofilm depths, suggesting effective excitation delivery (Fig. 3.7). Cell density decreased with biofilm depth, indicating more growth at the biofilm surface (Fig. 3.7). The FLIM phasor signal of masked cells or aggregates shifted with biofilm depth (Fig. 3.7, 3.8A). The biofilm surface FLIM signal was dominated by a longer lifetime species, and the sample phasor coordinates were near the phasor coordinates of reduced pyocyanin. It is also worth noting that this long lifetime signal was observed when a coverslip was placed on top of the biofilm sample. FLIM of the biofilm surface without a cover slip was acquired with an air objective, and indicated oxygen limitation was driving the formation of the long lifetime species believed to be reduced pyocyanin (data not shown). Lifetime unmixing of the biofilm samples (imaged with a coverslip) indicated higher contributions from reduced pyocyanin at the biofilm surface (Fig. 3.7, 3.8).

3.4 Discussion

Oxygen is scarce in many environments, and in the context of chronic infections, hypoxia drives microbes to produce redox-active metabolites that can act as alternative electron acceptors, but are also toxic and may contribute to disease progression. Bacterial biofilms have little oxygen beneath the surface. P. aeruginosa synthesizes and secretes redox-active pyocyanin to recycle electrons in low-oxygen [62]. We sought to determine the redox state of P. aeruginosa-produced pyocyanin throughout biofilms, and developed fluorescence imaging unmixing approach to calculate

pyocyanin abundance relative to other fluorescent metabolites.

3.4.1 FLIM and HIM unmixing results varied for fluorophores

FLIM phasor unmixing of the first harmonic was used to determine the contribution of four species - reduced pyocyanin, apo-pyoverdine, NADH, and enzyme-bound NADH - to fluorescent signals in P. aeruginosa biofilms (Fig. 3.3). To validate the FLIM unmixing results, we implemented an orthogonal method with HIM phasor-based unmixing of two harmonics. By incorporating additional harmonics, the system is sufficiently constrained and can theoretically be solved with HIM unmixing. However, there was very little modulation of intensity in the emission acquisition window (410-500 nm).The HIM data was truncated for two reasons: (1) to directly compare predictions from the HIM and FLIM approaches and (2) to avoid introducing additional fluorescent species, such as FAD and other phenazines [62], and potentially confounding the HIM analyses (Fig. 3.2). The HIM and FLIM-predicted fractional contributions did not correlate overall (Fig. 3.5,3.6). FLIM pyoverdine and NADH predictions contradicted with that of HIM. FLIM predicted large contributions from pyoverdine, while HIM predicted larger contributions from NADH in the same samples. The spectral phasor positions of pyoverdine and free NADH are close, likely contributing to the discordance between HIM and FLIM predictions. In addition, the fluorescence lifetime of pyoverdine (4 ns) and enzyme-bound NADH (reported to range from 1.7-9 ns (175, 179)) could overlap depending on local conditions. In contrast, reduced pyocyanin had a distinct HIM spectral phasor position and long lifetime FLIM phasor fingerprint (Fig. 3.3). The FLIM and HIM pyocyanin fractional contributions were similar and correlated with independent total pyocyanin measurements. We proceeded with the FLIM unmixing method to determine if pyocyanin fractional contributions shift throughout P. aeruginosa biofilms.

3.4.2 Reduced pyocyanin was localized at the biofilm surface in our system

To recapitulate slower bacterial growth observed in infections [77, 78], colony biofilms were radially grown for five days in artificial sputum medium with soft agar. The radial center of the colony was imaged axially to capture the different depths in the oldest population of the biofilm. Reasoning that natural gradients would form with less oxygen exposure deeper in the biofilm, we initially hypothesized that P. aeruginosa would produce more pyocyanin in the hypoxic core of the biofilm [61, 62, 79]. However, in our system, reduced pyocyanin dominated the FLIM signal at the surface of the biofilm Fig. 3.7, 3.8, and the pyocyanin-dominant signal was only observed when imaging with a coverslip placed on top of the sample. The highest density of P. aeruginosa growth was at the surface and was associated with the reduced pyocyanin FLIM signal Fig. 3.7. After oxygen was limited by the introduction of a coverslip at the surface, dense populations utilized a pool of pyocyanin for electron recycling. Our biofilm model agrees with previous studies showing that population density controls phenazine biosynthesis [80, 81] and oxygen is required for pyocyanin biosynthesis [82]. Although it may seem counterintuitive that oxygen is necessary to synthesize an alternative electron acceptor, pyocyanin has the highest affinity for oxygen out of other studied phenazines [63]. In locally anoxic conditions, P. aeruginosa couples pyocyanin reduction with oxidation of glucose and pyruvate, which generates ATP and increases anaerobic survival [62, 83, 84]. The reduced pyocyanin is secreted and oxidized extracellularly [62, 79]. A portion of the pyocyanin can be retained in the biofilms by P. aeruginosa-derived extracellular DNA that binds to phenazines [85, 86], distributing pyocyanin both inside and outside of the biofilm and enabling electron cycling.

3.5 Limitations and future directions

The phasor approach has several benefits, including a clear visualization of the data and reliable deconvolution of the instrument response function [87]. The phasor transform effectively applies a bandpass filter to the data, compressing the complete time-domain (or wavelength-domain) signal into two numbers, the s and g components. The first harmonic contains the low frequency components of the signal, representing an approximation to the shape of the lifetime (or spectrum) trace with a single sine or cosine function. The addition of higher harmonics further refines the shape of the signal. The approach decreases the influence of high-frequency noise, giving an advantage over direct least-squares unmixing approaches. A consideration in the application of the simultaneous spectral-lifetime unmixing method is that the spectral range of acquisition must be nearly identical for the two measurements. For accurate unmixing, the spectral ranges need to have broad enough modulation in the pure species. If the spectral range is too narrow (as in our measurements), the difference in the shape between pure species is negligible. One of the challenges in unmixing the FLIM and HIM images using spectrum and lifetime simultaneously is that each pixel in the FLIM image must be aligned with the HIM image. With our instrument, the Zeiss LSM 880, acquisition of FLIM images was delayed by a couple minutes relative to spectral acquisition due to the need to switch to a different data acquisition software. During this time, bacteria in the sample can produce new metabolites. The unmixing method yields the fractional contributions of fluorophores in each pixel in an image, and its accuracy is dependent on the fluorophores used as the references. While several studies on bacterial FLIM have been conducted, the lifetime of NADH when bound to bacteria enzymes has not been well-characterized. We used 2.8 ns to represent all enzyme-bound NADH in our unmixing program, but the lifetime of NADH changes in different enzymes and local environments [72, 76, 88]. Finally, the fractional contributions are proportional to the relative concentrations of various metabolites. With appropriate instrumentation and characterization of fluorophores, it is possible measure the absolute concentration of molecules [89].

3.6 Conclusions

Here, we compared two orthogonal measurements to determine the presence and relative amount of reduced pyocyanin in P. aeruginosa biofilms. Although our implementation is far from perfect, it puts forward a framework to combine hyperspectral imaging and lifetime imaging and map out the concentrations of different fluorophores in a sample with high molecular specificity.

3.7 Methods and Materials

3.7.1 Chemicals and bacterial media

HPLC-grade pyocyanin was ordered from Sigma-Aldrich (P0046). 10 mM stocks were dissolved in 20% ethanol and stored at -20°C. Artificial sputum and M9 minimal media with 40 mM succinate soft agar were used to grow P. aeruginosa biofilms. The recipes for both media types were modified from Gao et al. [90] to include 0.28% final agar concentration. To visualize biofilm colony growth over time, the agar was prepared in large petri dishes (150x15 mm).

3.7.2 Bacterial strains and growth

P. aeruginosa PA14 and the phenazine knockout phzA1-G1/A2-G2 were obtained from Dianne Newman's lab at California Institute of Technology. For biofilm imaging, the bacteria were grown overnight on Todd-Hewitt agar, and individual colonies were inoculated into the center of the artificial sputum or M9 succinate soft agar plates. The biofilm colonies were grown aerobically at 37°C for 5 days.

Chemical reduction of 1-hydroxyphenazine and pyocyanin and electrochemical reduction of py-

ocyanin. Five hundred micromolar stocks of pyocyanin were diluted in 1X MOPS buffer with concentration gradients of TCEP ranging from 0.1 mM to 125 mM (pH 7). A fresh stock of 821μM of pyocyanin was prepared in ammonium acetate 0.1M KCl MOPS buffered solution in and electrochemically reduced following the protocol developed by Wang and Newman (165). The electrochemical cell consisted of a glassy carbon working electrode, platinum wire counter electrode, and Ag/AgCl2 reference electrode. The voltage was set to -0.345V, and the reaction proceeded in an anaerobic chamber overnight until the current reached zero. For 1-hydroxyphenazine, 500 micromolar stocks were prepared and diluted in 1XMOPS buffer with pH 7-buffered DTT as the reducing agent [91].

3.7.3 Hyperspectral and fluorescence lifetime imaging on Zeiss LSM-880

In order to characterize the emission spectra and fluorescence lifetime of NADH, FAD, pyoverdine, reduced pyocyanin, and reduced 1-hydroxyphenazine, solutions were transferred to a slide. The reduced pyocyanin and 1-hydroxyphenazine were prepared in a Coy anaerobic chamber and sealed with iSpacers to avoid oxygen exposure (https://www.sunjinlab.com/).

Biofilms grown in the artificial sputum and M9 succinate soft agar were cut with a sterile razor and placed onto a MATTEK dish (Part No: P35G-1.5-14-C) with the surface of the biofilm on the coverslip. To compare the impact of oxygen on the spectral and lifetime signal, the biofilm samples were (1) placed in a dish open to air and immediately imaged or (2) were placed in between two coverslips and sealed in the dish with tape to promote oxygen consumption for 2h.

The pure fluorophore solutions and biofilm surfaces were imaged on an inverted Zeiss LSM-880 with an ISS Spartan3 FLIMbox, BH HPM-100-40-Hybrid detector, and a Spectra Physics Mai Tai titanium sapphire laser. The fluorophores were excited with 2-photon excitation at 740 nm and laser power ranging from 1-10 mW. For the hyperspectral imaging, emission ranging from 410-695 nm was collected with 9 nm step resolution over 32 channels. One frame was collected per sample with

a pixel dwell time of 4 µs. The spectra were analyzed on Zeiss Zen software, and .lsm files were exported for downstream deconvolution steps. After collecting the spectra, fluorescence lifetime of the same sample was obtained by switching the light path to the FLIMbox detectors. The sample was excited with the same wavelength and laser power as the spectral images. The emission was filtered with a 495 nm LP dichroic and Semrock 442/46 nm BrightLine single-band bandpass filter (CFW-BP01-Clin-25). The fluorescence lifetime data was acquired using SimFCS4. To obtain enough fluorescence lifetime signal for the downstream analysis, 10-30 frames were collected per sample, with a frame size of 256x256 pixels and pixel dwell time of 32 µs.

3.7.4 Z-stack fluorescence lifetime of biofilms on the DIVER microscope

Intact P. aeruginosa biofilms were prepared for z-stack imaging by adding a large coverslip on top of the surface of the biofilm, and then imaged with a 0.8 NA 40x Water objective. As a control, biofilms without a coverslip were also imaged using an 0.45 NA 20x air objective. Z-stacks were obtained on a custom-made microscope at the Laboratory for Fluorescence Dynamics, the DIVER (Deep Imaging Via Enhanced Recovery) [10]. The DIVER is a Nikon Eclipse TE2000-U microscope equipped with a wide-area 18x18 mm photomultiplier tube (PMT) (Hamamatsu R7600P-300) which enhances photon collection. Samples were excited with 2-photon excitation at 740 nm using a Tsunami Spectra-Physics Ti:Sapphire laser (80 MHz). The emission was filtered with a Schott BG-39 filter and NADH-targeted optical bandpass filter (400-500 nm). The fluorescence lifetime data was collected with SimFCS v4 software. Z-stacks were automatically acquired every 50-100 µm from the surface of the biofilm to 2 mm deep. The laser power was increased with an exponential function for deeper sample imaging, with the power ranging from 1-58 mW.

3.7.5 Fluorescence lifetime analysis and visualization

The fluorescence lifetime data was analyzed in SimFCS4 software using the phasor approach [73]. The phasor approach uses a cosine-sine discrete fast Fourier transform to transform raw fluorescence lifetime traces onto a two-coordinate polar phasor plot. The resulting g and s coordinates are the cosine and sine components of the transform for a given frequency (80 MHz). The fluorescence lifetime images were processed following protocols in Ranjit *et al.* [87]. The images were first masked using fluorescence intensity thresholds to exclude pixels with background signal (see Supplemental). The resulting images contain the fluorescence lifetime phasor coordinates for each pixel. For the single cell or cluster analyses, individual cells or group of cells were selected as regions of interest, and the average g and s values were calculated.

3.7.6 Unmixing of fluorescence lifetime and hyperspectral data

To represent the fluorescence lifetime data in phasor space, the intensity trace is Fourier transformed to obtain the s and g coordinates at a harmonic n,

$$s(n) = \frac{\int_{T_0}^{T_1} I(t)\sin(2\pi n\frac{t-T_0}{T_1-T_0})dt}{\int_{T_0}^{T_1} I(t)dt} \tag{3.1}$$

$$g(n) = \frac{\int_{T_0}^{T_1} I(t)\cos(2\pi n\frac{t-T_0}{T_1-T_0})dt}{\int_{T_0}^{T_1} I(t)dt} \tag{3.2}$$

Similarly, the spectrum is transformed with the equations

$$s(n) = \frac{\int_{\lambda_0}^{\lambda_1} I(\lambda)\sin(2\pi n\frac{\lambda-\lambda_0}{\lambda_1-\lambda_0})d\lambda}{\int_{\lambda_0}^{\lambda_1} I(\lambda)d\lambda} \tag{3.3}$$

$$g(n) = \frac{\int_{\lambda_0}^{\lambda_1} I(\lambda)\cos(2\pi n\frac{\lambda-\lambda_0}{\lambda_1-\lambda_0})d\lambda}{\int_{\lambda_0}^{\lambda_1} I(\lambda)d\lambda} \tag{3.4}$$

The pure fluorophores predicted to be present in the sample are characterized by spectral and lifetime imaging, creating a basis set of k - pure components in the lifetime and spectral phasor space, at each harmonic n:

$$S_{\text{basis}}, G_{\text{basis}}(n) = \{(s_{t1}, g_{t1}), ...(s_{ti}, g_{ti}); (s_{\lambda 1}, g_{\lambda 1}), ...(s_{\lambda i}, g_{\lambda i})\}_n \tag{3.5}$$

The measured signal in each pixel of the image is given by

$$S_{\text{signal}}, G_{\text{signal}}(n) = \{(s_{t\text{signal}}, g_{t\text{signal}}), (s_{\lambda\text{signal}}, g_{\lambda\text{signal}})\}_n \tag{3.6}$$

In the absence of FRET or other non-linear effects, and if the spectral window for FLIM acquisition is the same as the spectral window for hyperspectral acquisition, the measured signal is modeled as the sum of the each of the components of the basis set, multiplied by the fractional contribution f_j,

$$S_{\text{model}}(n) = \sum_{j=1}^{k} s_{j,n} \cdot f_j \tag{3.7}$$

$$G_{\text{model}}(n) = \sum_{j=1}^{k} g_{j,n} \cdot f_j \tag{3.8}$$

The fractional contributions best describing the signal are found by least squares global optimiza-

tion:

$$\vec{f} = \text{argmin}_f \left\{ \sum_n \left(S_{\text{model}}(\vec{f}, n) - S_{\text{signal}}(n) \right)^2 + \sum_n \left(G_{\text{model}}(\vec{f}, n) - G_{\text{signal}}(n) \right)^2 \right\} \tag{3.9}$$

With the constraint that the sum of all fractions f_i is 1,

$$\sum_i f_i = 1 \tag{3.10}$$

The optimization routine used in this work is simplicial homology global optimization [92]. The number of harmonics that can be used in the unmixing algorithm is determined by the resolution of the spectral or lifetime instrument. If too many harmonics are used, the data becomes too noisy and the model breaks down. The maximum number of harmonics that can be used is limited by the Nyquist frequency of the instrument as well as the signal modulation. If there is no modulation in the signal, the phasor coordinates become smaller than the variance introduced by the noise, and unmixing becomes impossible. The unmixing program is open-source and available at: https://github.com/tgallagh/HyperFluo

Example of P. aeruginosa PA14 biofilm images. Fluorescence intensity of the biofilm at different depths - surface or 0 to 500 µm deep (column 1). The fluorescence lifetime color map projections, where cooler colors are indicative of longer lifetimes (column 2). The predicted fractional contributions of the four fluorophores indicates high abundance of reduced pyocyanin at the surface relative to the other species. Scale bar = 20 µm

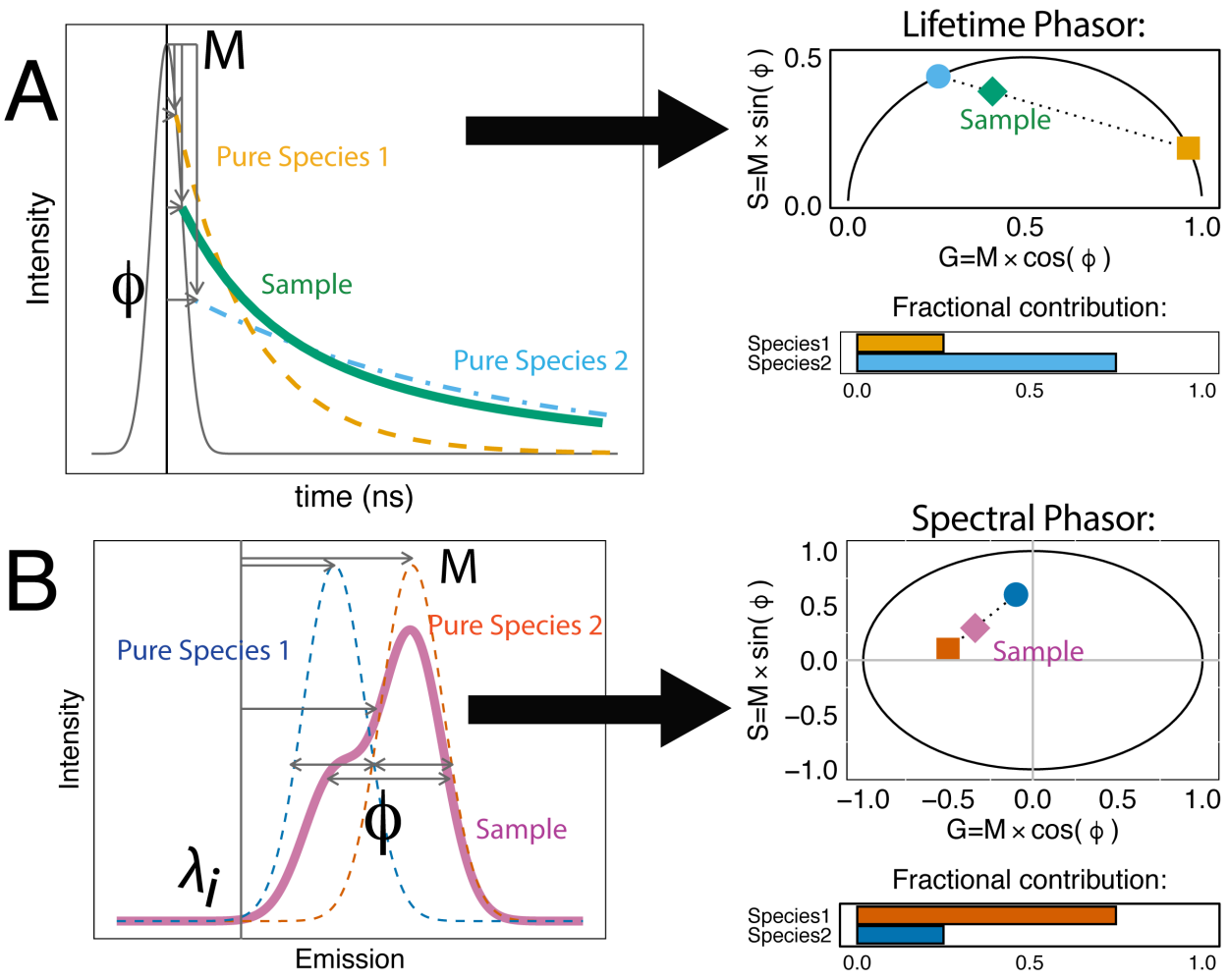

Figure 3.1: The phasor families are a powerful approach for analyzing and visualizing fluorescence data and facilitate calculations of relative abundances of fluorescent species in samples. (A) A simplified representation of the transformation of fluorescence exponential decays (left) into the fluorescence lifetime phasor (right). A Fourier transform is used to calculate the modulation (M) and phase shift (ϕ) relative to the laser pulse excitation source. M and ϕ are represented graphically for two pure fluorophores (orange dash line, blue dash-dot line) and a sample containing a mix of the two species (green solid line). The phasor G and S coordinates are the cosine and sine components of the Fourier transforms. Species closer to the origin of the phasor have long lifetimes, whereas species on the right corner of the phasor have short lifetimes. The fractional contribution of fluorescent species 1 (orange square) and species 2 (blue circle) to a sample (green diamond) can be determined algebraically if the lifetime of the pure species is known. (B) Example emission spectra from three fluorescent samples, including pure species and a sample with a mix of the two species (middle spectrum). A Fourier transform of the spectra gives ϕ, which represents the spectrum width, and M, which represents the spectral shift relative to the first wavelength measurement (λ). Species closer to the inner circle have broader emission spectra.

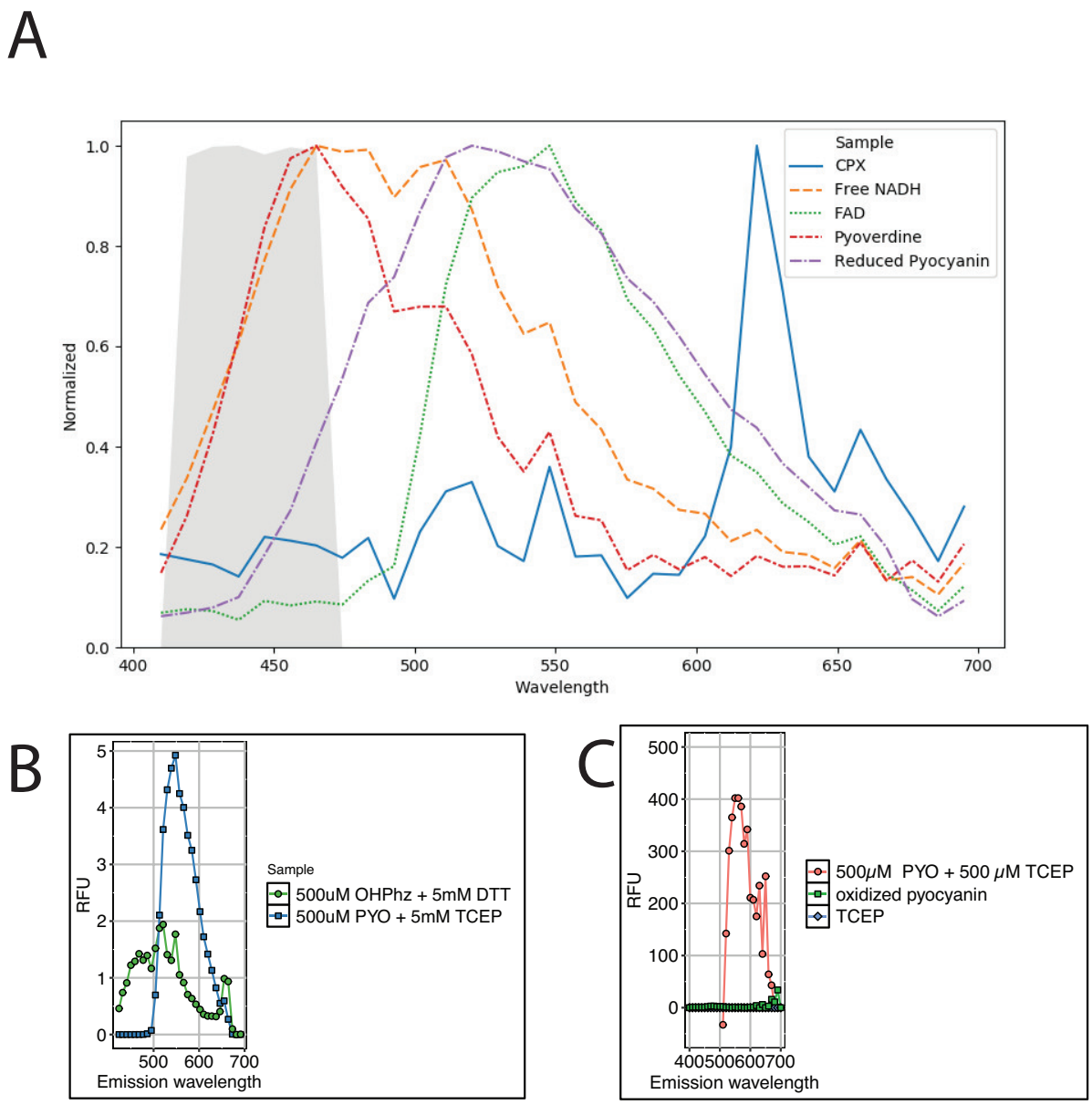

Figure 3.2: (A) Two-photon emission spectra, normalized by the max peak intensity, of some of the fluorescent metabolites produced by P. aeruginosa. (B) Emission spectrum of chemically reduced 1-hydroxy-phenazine and pyocyanin (0.5 mM of phenazine with 5 mM of reducing agent). (C) Emission spectra of reduced pyocyanin (0.5 mM pyocyanin with 0.5 mM TCEP), oxidized pyocyanin (0.5 mM), and background from buffer (TCEP). Oxidized pyocyanin had negligible fluorescent with two-photon excitation at 740 nm.

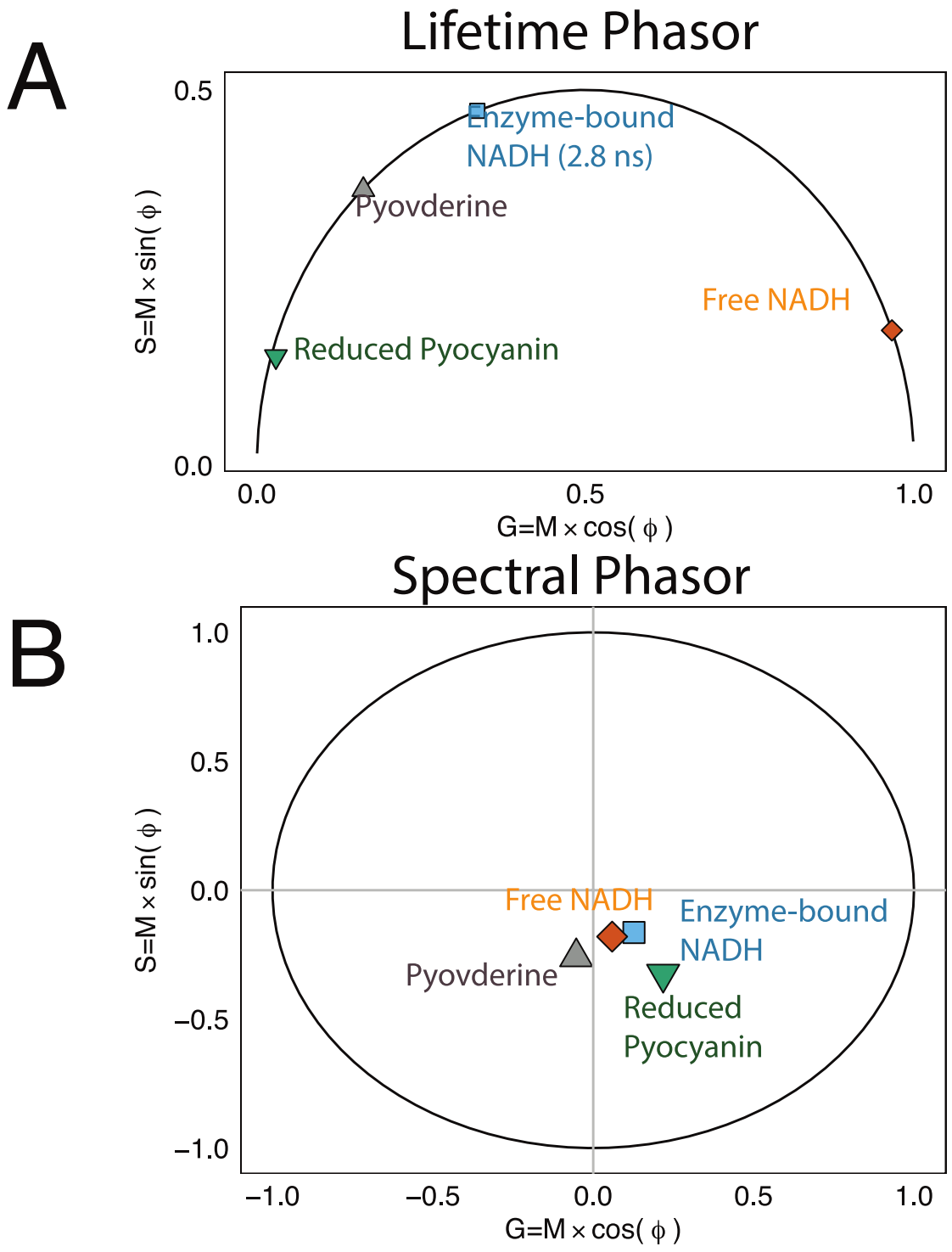

Figure 3.3: (A) Fluorescence lifetime and (B) spectral phasor of pure fluorescent species (first harmonics). For the fluorescence lifetime phasor, the S and G components were calculated for a lifetime of 2.8 ns and used as the reference for enzyme-bound NADH (Fig. 3.9). For the spectral phasor, the emission spectra were obtained over 9 channels from 410-486 nm.

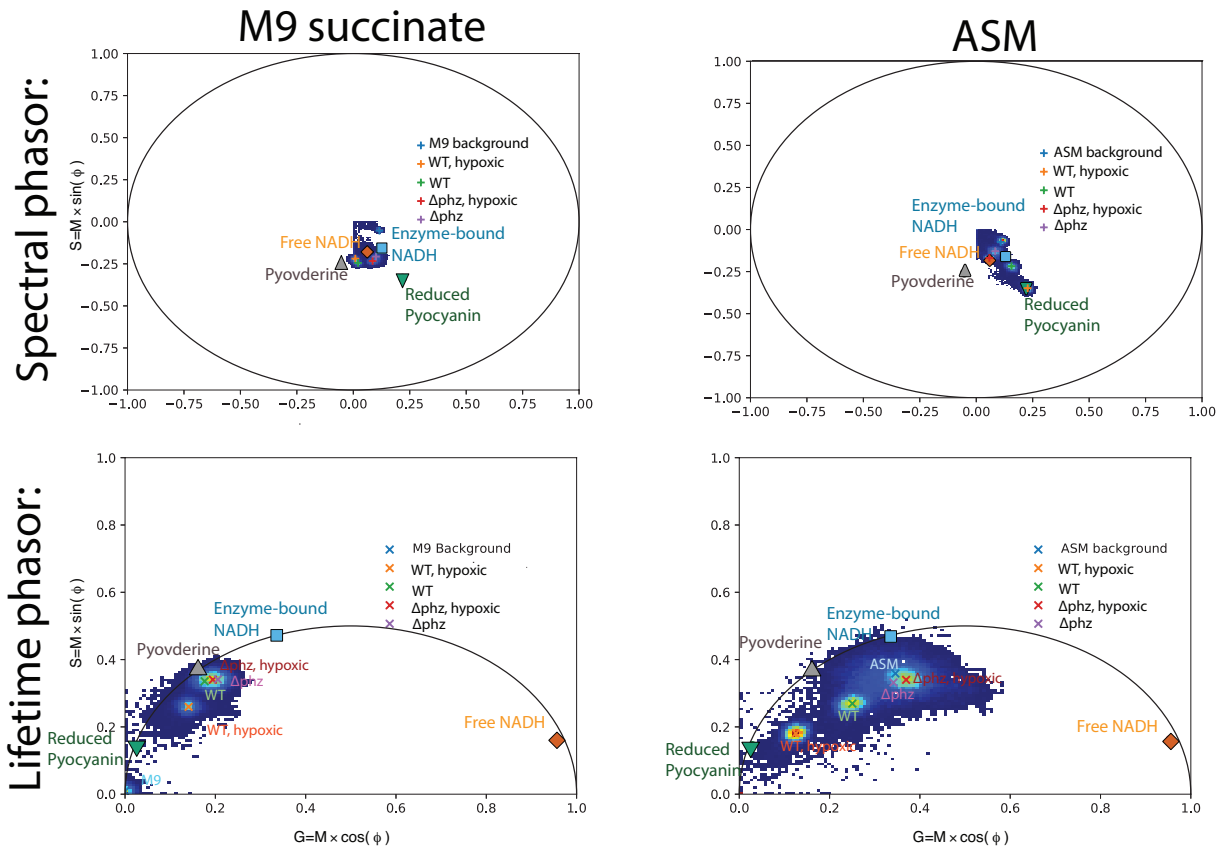

Figure 3.4: Fluorescence lifetime and spectral phasor of WT P. aeruginosa and a null phenazine mutant grown in aerobic and hypoxic conditions in M9 succinate and artificial sputum medium.

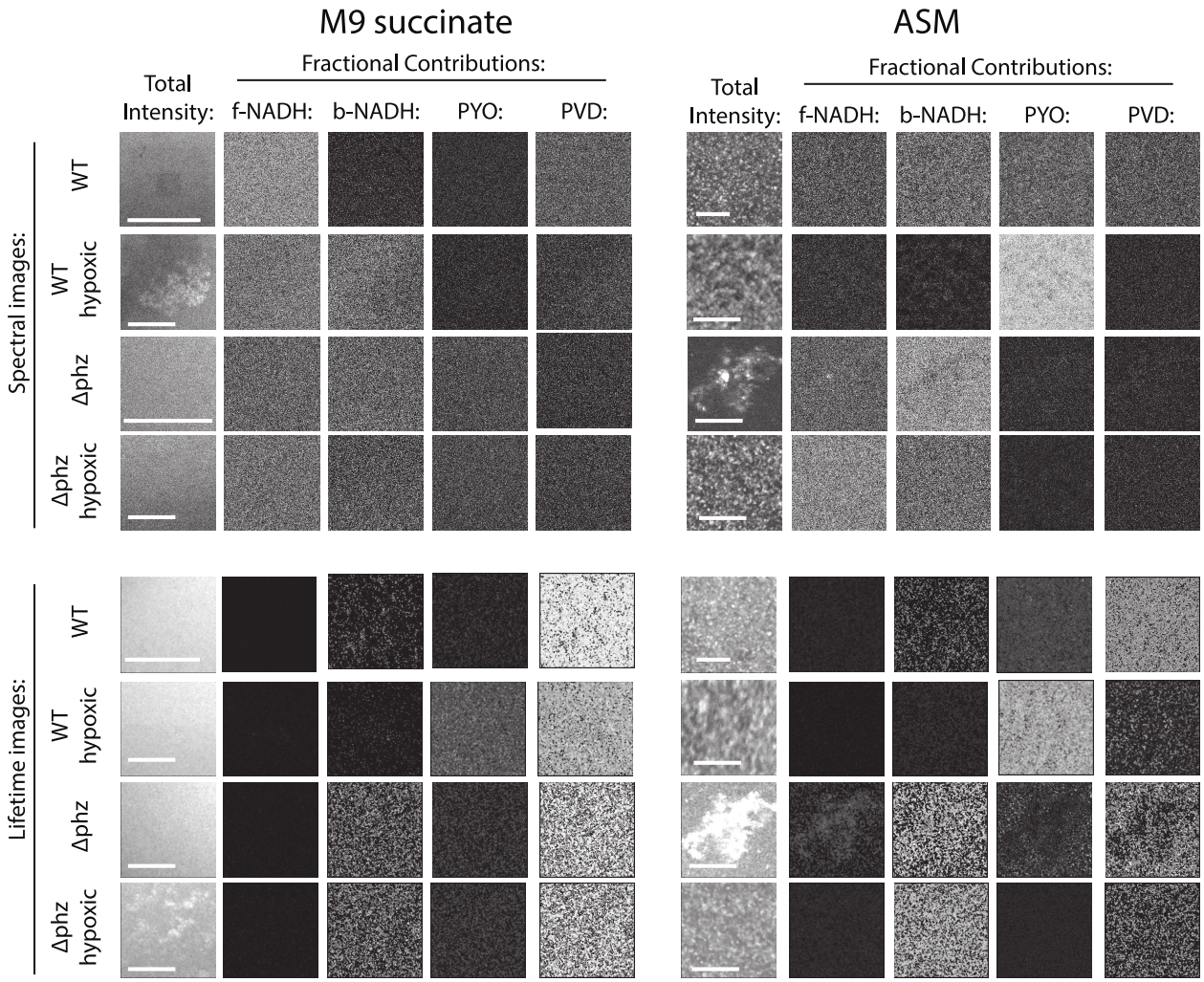

Figure 3.5: WT P. aeruginosa and a null phenazine mutant grown in aerobic and low oxygen conditions in M9 succinate and artificial sputum medium. The fluorescence intensity of the images are depicted in the 1st columns. The predicted fractional contributions of four fluorophores (free NADH, enzyme-bound NADH, reduced pyocyanin, and apo-pyoverdine) from lifetime and spectral phasor data. Scale bar=20 μm.

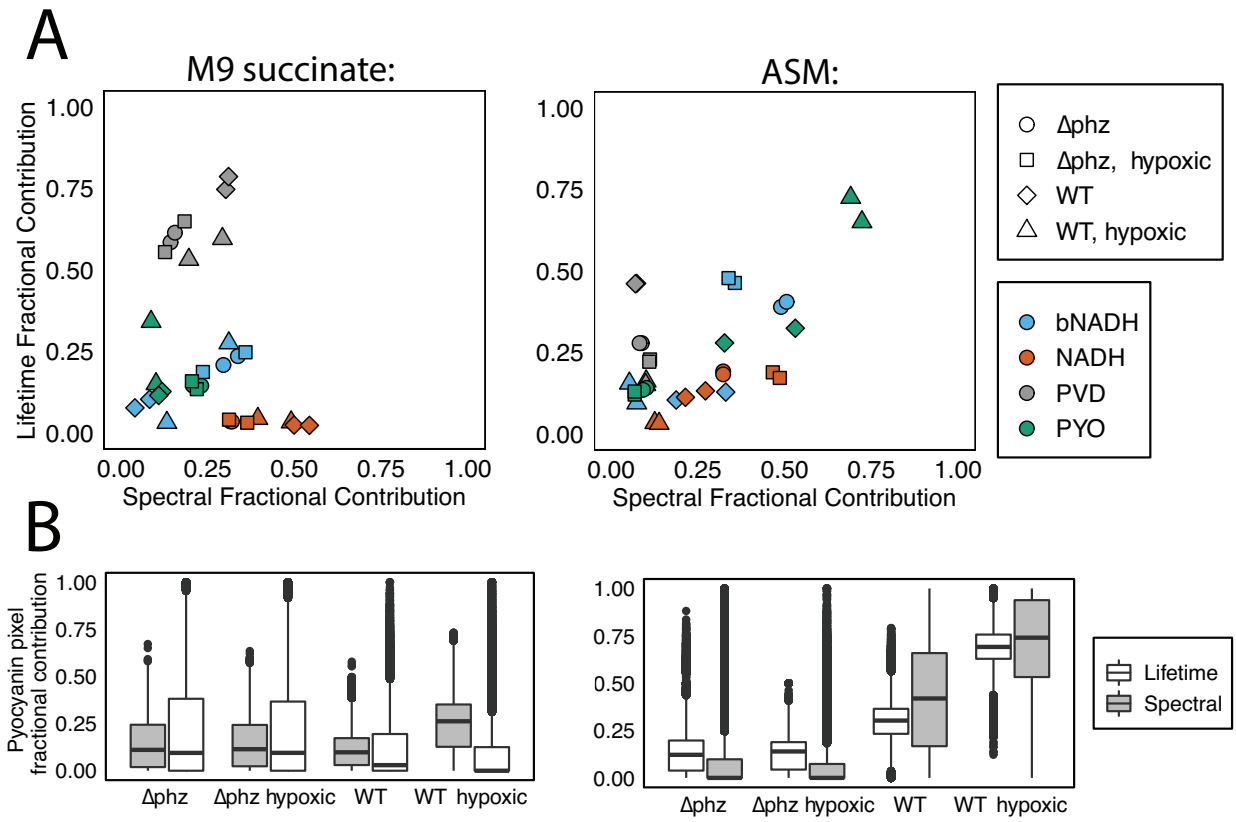

Figure 3.6: (A) The spectral and fluorescence lifetime fractional contribution predictions do not correlate for M9 succinate cultures (r=-0.22, df = 30, p-value = 0.2) and moderately correlate (r=0.6, df = 30, p-value < 0.05) for artificial sputum medium cultures. (B) In cultures with high pyocyanin production (WT and WT hypoxic in ASM), the lifetime and spectral predicted fractional contributions of pyocyanin were similar.

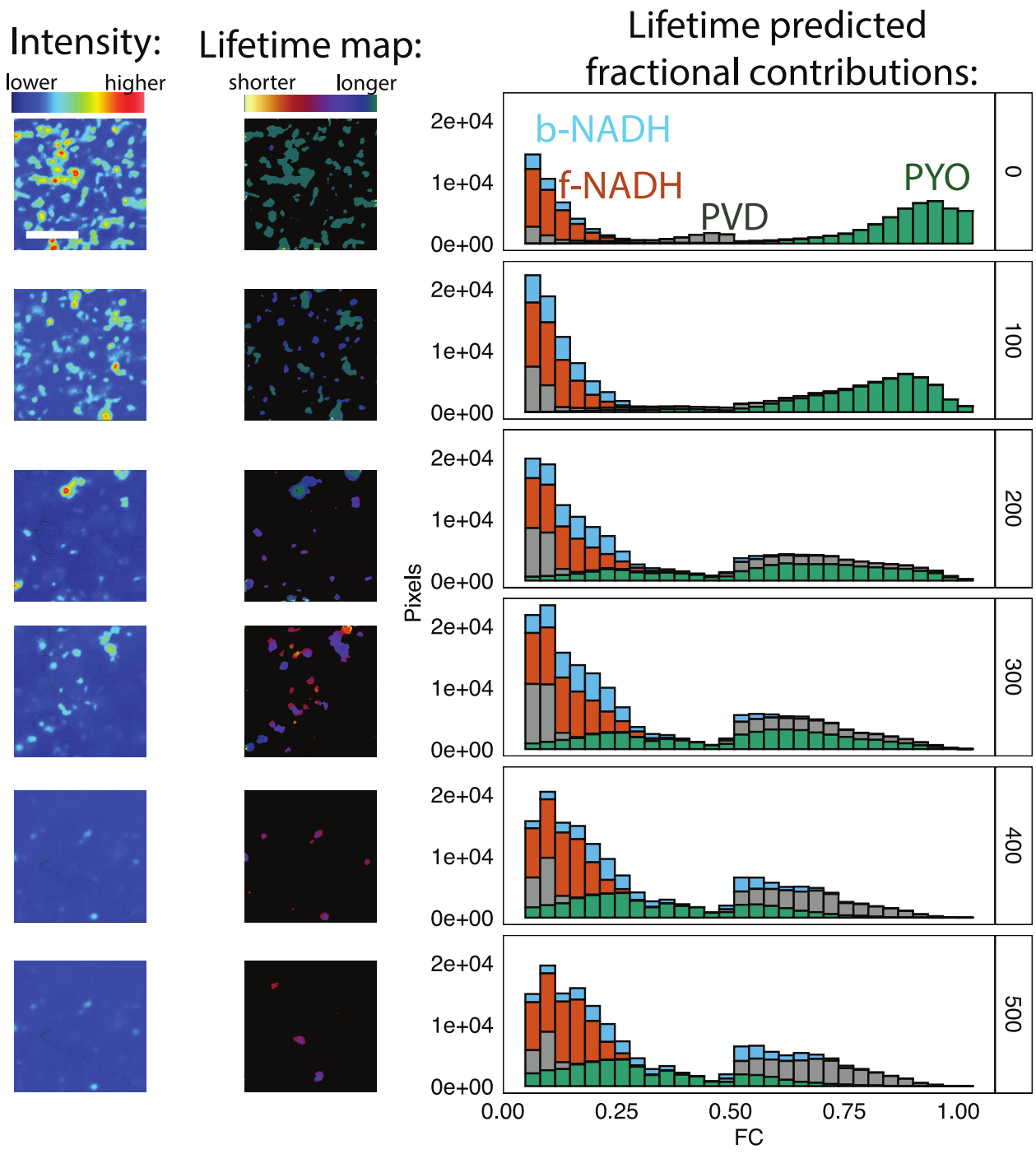

Figure 3.7: (A) Fluorescence lifetime phasor of PA14 biofilms in artificial sputum medium at different depths (0=surface). (B) Pyocyanin fractional contributions at different depths in the biofilm. N=5 biofilm plates.

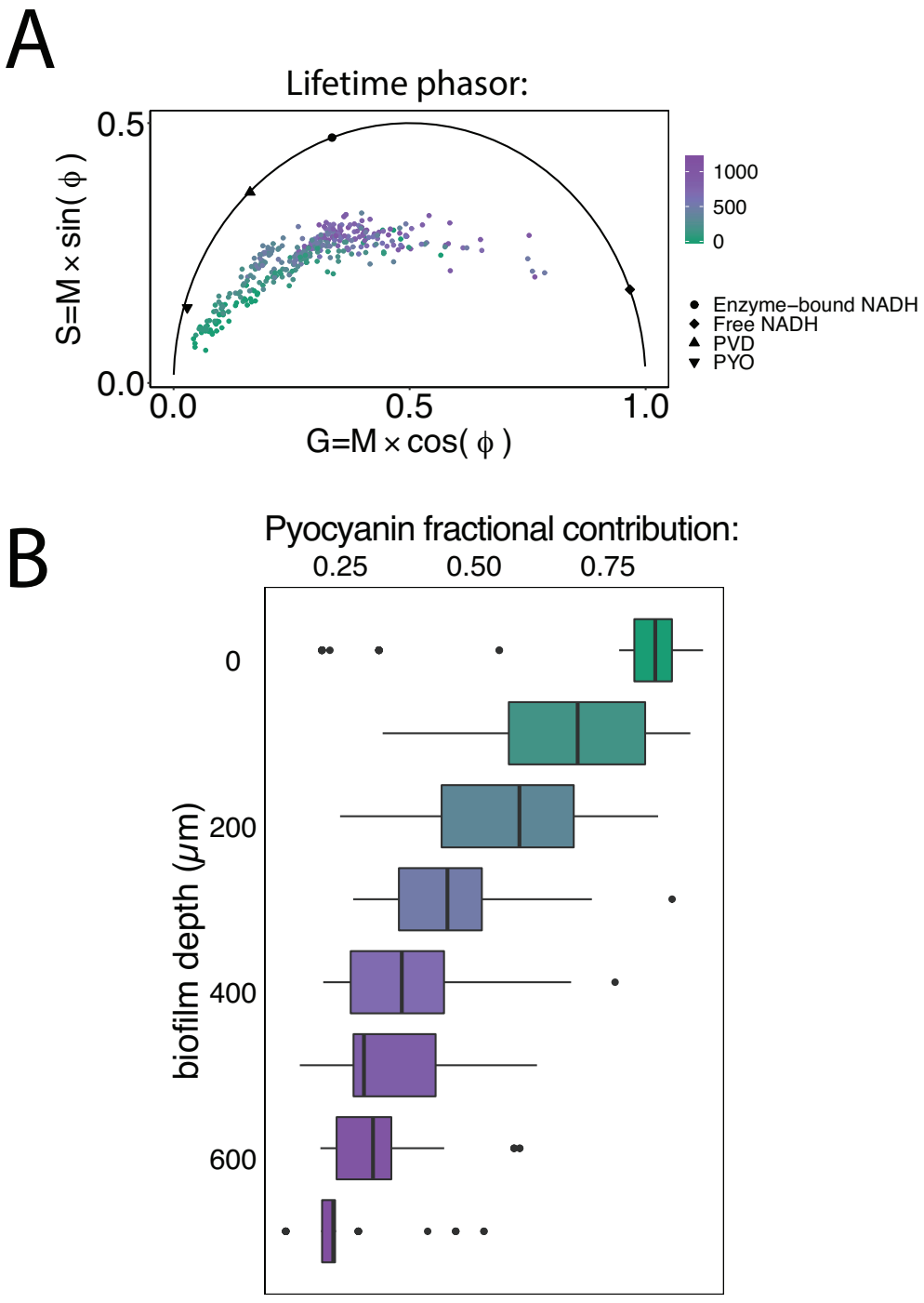

Figure 3.8: (A) Fluorescence lifetime phasor of PA14 biofilms in artificial sputum medium at different depths (0=surface). (B) Pyocyanin fractional contributions at different depths in the biofilm. N=5 biofilm plates.

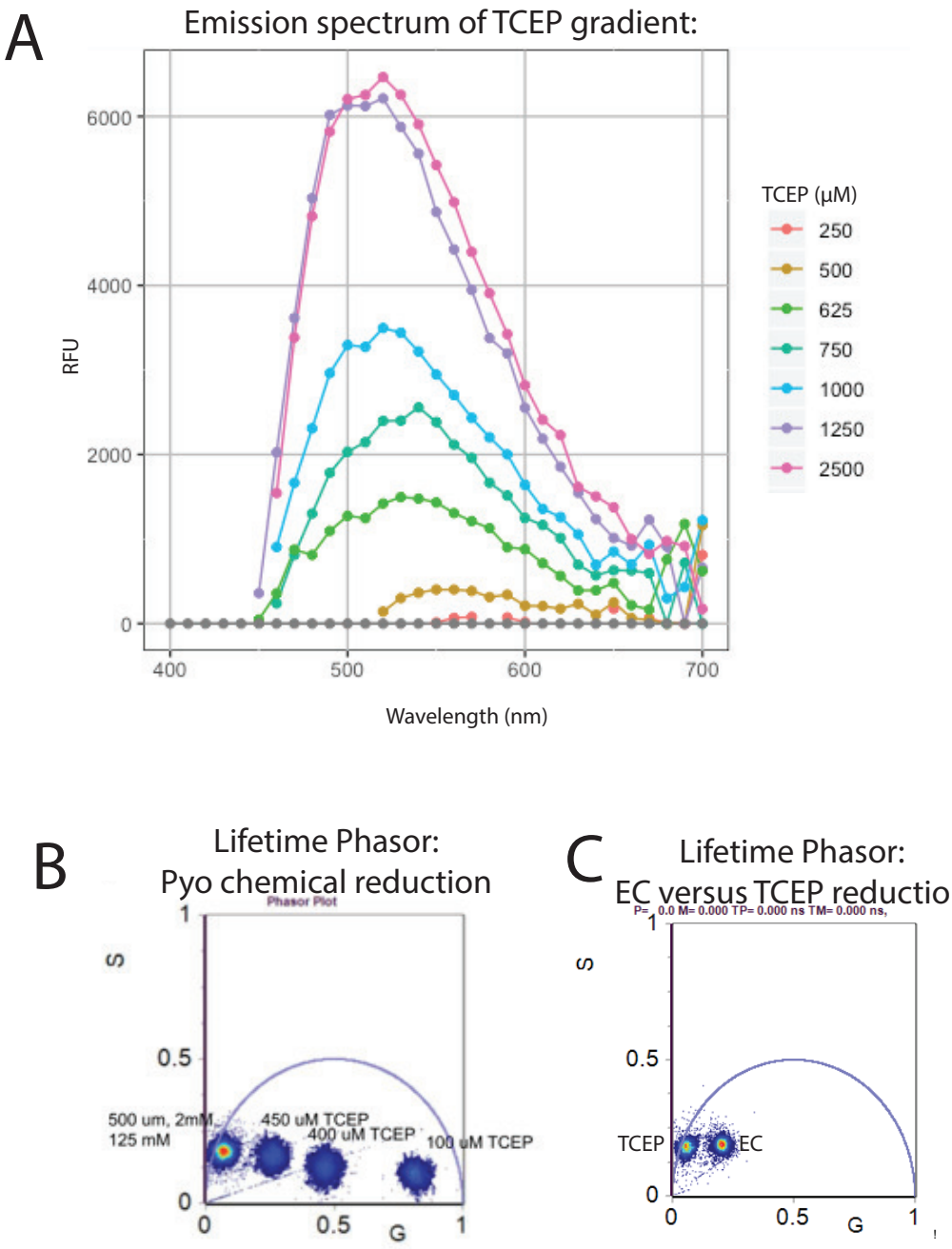

Figure 3.9: (A) The emission spectra of pyocyanin shifts to the right with higher concentrations of reducing agent (TCEP). The samples were prepared in a 96-well plate with 0.5 mM of pyocyanin and titrations of TCEP in an anaerobic chamber. The spectra were acquired using 1-photon fluorescence excitation (370 nm) on a fluorometer. (B) The FLIM phasor position of pyocyanin (0.5 mM) varies with different concentrations of TCEP reducing agent. (C) FLIM phasor positions of electrochemically-reduced pyocyanin (0.821 mM) compared to 1 mM TCEP reduced pyocyanin (0.5 mM). FLIM data in B and C were acquired with 2-photon fluorescence excitation at 740 nm and an emission filter of 442/46 nm.

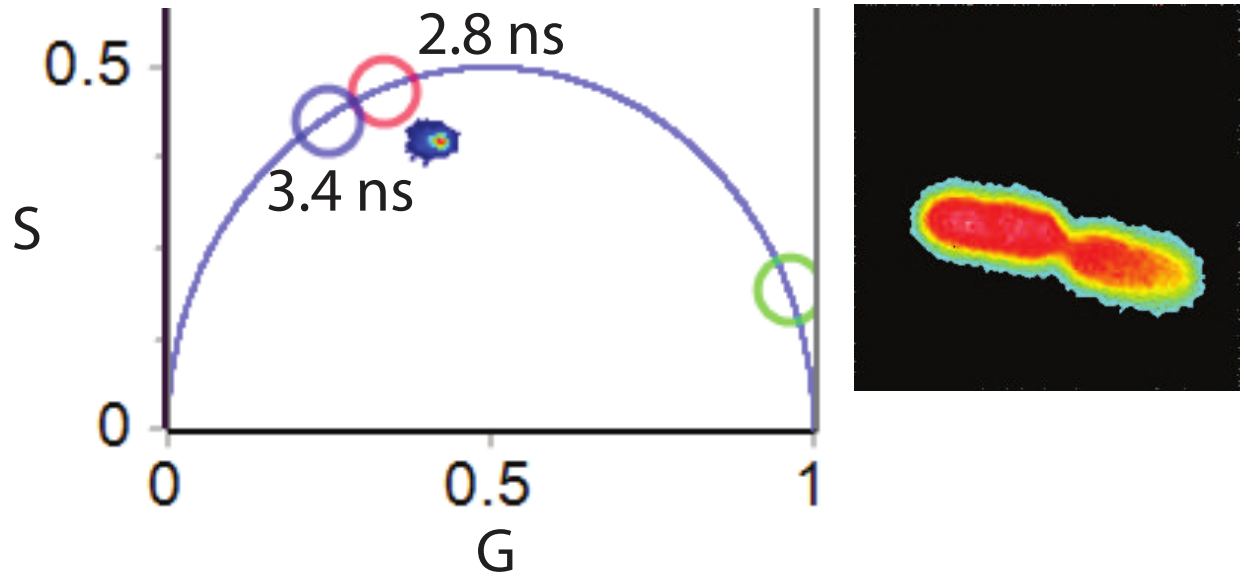

Figure 3.10: The fluorescence lifetime of a single cell P. aeruginosa grown in aerobic M9 glucose for 24h.

Bibliography

[1] Alexander Dvornikov and Enrico Gratton. Imaging in turbid media: a transmission detector gives 2-3 order of magnitude enhanced sensitivity compared to epi-detection schemes. *Biomedical Optics Express*, 7(9):3747, 2016.

[2] C Xu, W Zipfel, J B Shear, R M Williams, and W W Webb. Multiphoton fluorescence excitation: new spectral windows for biological nonlinear microscopy. *Proceedings of the National Academy of Sciences of the United States of America*, 93(20):10763–8, oct 1996.

[3] Rebecca M Williams, Warren R Zipfel, and Watt W Webb. Multiphoton microscopy in biological research. *Current opinion in chemical biology*, 5(5):603–608, 2001.

[4] David R. Miller, Jeremy W. Jarrett, Ahmed M. Hassan, and Andrew K. Dunn. Deep tissue imaging with multiphoton fluorescence microscopy. *Current Opinion in Biomedical Engineering*, 4:32–39, dec 2017.

[5] Fritjof Helmchen and Winfried Denk. Deep tissue two-photon microscopy, dec 2005.

[6] Patrick Theer and Winfried Denk. On the fundamental imaging-depth limit in two-photon microscopy. *Journal of the Optical Society of America A*, 23(12):3139, 2006.

[7] Warren R. Zipfel, Rebecca M. Williams, Richard Christiet, Alexander Yu Nikitin, Bradley T. Hyman, and Watt W. Webb. Live tissue intrinsic emission microscopy using multiphoton-excited native fluorescence and second harmonic generation. *Proceedings of the National Academy of Sciences of the United States of America*, 100(12):7075–7080, 2003.

[8] Kwanghun Chung, Jenelle Wallace, Sung-Yon Kim, Sandhiya Kalyanasundaram, Aaron S Andalman, Thomas J Davidson, Julie J Mirzabekov, Kelly A Zalocusky, Joanna Mattis, Aleksandra K Denisin, Sally Pak, Hannah Bernstein, Charu Ramakrishnan, Logan Grosenick, Viviana Gradinaru, and Karl Deisseroth. Structural and molecular interrogation of intact biological systems. *Nature*, 497(7449):332–337, 2013.

[9] Viera Crosignani, Alexander Dvornikov, Jose S Aguilar, Chiara Stringari, Robert Edwards, William W. Mantulin, and Enrico Gratton. Deep tissue fluorescence imaging and in vivo biological applications . *Journal of Biomedical Optics*, 17(11):116023, 2012.

[10] Alexander Dvornikov, Leonel Malacrida, and Enrico Gratton. The DIVER Microscope for Imaging in Scattering Media. *Methods and protocols*, 2(2):53, jun 2019.

[11] John A Nelder and Roger Mead. A simplex method for function minimization. *The computer journal*, 7(4):308–313, 1965.

[12] William H Press, Saul A Teukolsky, William T Vetterling, and Brian P Flannery. *Numerical recipes 3rd edition: The art of scientific computing*. Cambridge university press, 2007.

[13] Amanda J Wright, David Burns, Brett A Patterson, Simon P Poland, Gareth J Valentine, and John M Girkin. Exploration of the optimisation algorithms used in the implementation of adaptive optics in confocal and multiphoton microscopy. *Microscopy Research and Technique*, 67(1):36–44, 2005.

[14] Jianyong Tang, Ronald N. Germain, and Meng Cui. Superpenetration optical microscopy by iterative multiphoton adaptive compensation technique. *Proceedings of the National Academy of Sciences of the United States of America*, 109(22):8434–8439, 2012.

[15] Na Ji. Adaptive optical fluorescence microscopy. *Nature Methods*, 14(4):374–380, 2017.

[16] Martin Booth. Wave front sensor-less adaptive optics: a model-based approach using sphere packings. *Optics Express*, 14(4):1339, 2006.

[17] Delphine Débarre, Edward J Botcherby, Tomoko Watanabe, Shankar Srinivas, Martin J Booth, and Tony Wilson. for two-photon microscopy. 34(16):2495–2497, 2009.

[18] Na Ji, Daniel E. Milkie, and Eric Betzig. Adaptive optics via pupil segmentation for high-resolution imaging in biological tissues. *Nature Methods*, 7(2):141–147, 2010.

[19] Jacopo Antonello, Tim van Werkhoven, Michel Verhaegen, Hoa H. Truong, Christoph U. Keller, and Hans C. Gerritsen. Optimization-based wavefront sensorless adaptive optics for multiphoton microscopy. *Journal of the Optical Society of America A*, 31(6):1337, 2014.

[20] Xiaodong Tao, Justin Crest, Shaila Kotadia, Oscar Azucena, Diana C Chen, William Sullivan, and Joel Kubby. Live imaging using adaptive optics with fluorescent protein guide-stars. *Optics express*, 20(14):15969–82, 2012.

[21] Seokchan Yoon, Moonseok Kim, Mooseok Jang, Youngwoon Choi, Wonjun Choi, Sungsam Kang, and Wonshik Choi. Deep optical imaging within complex scattering media. *Nature Reviews Physics*, 2(3):141–158, 2020.

[22] Kai Wang, Wenzhi Sun, Christopher T Richie, Brandon K Harvey, Eric Betzig, and Na Ji. Direct wavefront sensing for high-resolution in vivo imaging in scattering tissue. *Nature communications*, 6:7276, 2015.

[23] K. M. Berland, P. T. So, and E. Gratton. Two-photon fluorescence correlation spectroscopy: method and application to the intracellular environment. *Biophysical Journal*, 68(2):694–701, 1995.

[24] M. J. Booth, M. A.A. Neil, and T. Wilson. Aberration correction for confocal imaging in refractive-index- mismatched media. *Journal of Microscopy*, 192(2):90–98, 1998.

[25] Delphine Débarre, Edward J Botcherby, Tomoko Watanabe, Shankar Srinivas, Martin J Booth, and Tony Wilson. Image-based adaptive optics for two-photon microscopy. *Optics letters*, 34(16):2495–2497, 2009.

[26] Martin J Booth. Adaptive optical microscopy: the ongoing quest for a perfect image. *Light: Science & Applications*, 3(4):e165—-e165, 2014.

[27] Michael X Henderson, Eli J Cornblath, Adam Darwich, Bin Zhang, Hannah Brown, Ronald J Gathagan, Raizel M Sandler, Danielle S Bassett, John Q Trojanowski, and Virginia M Y Lee. Spread of α-synuclein pathology through the brain connectome is modulated by selective vulnerability and predicted by network analysis. *Nature Neuroscience*, 22(8):1248–1257, 2019.

[28] Per Niklas Hedde, Leonel Malacrida, Siavash Ahrar, Albert Siryaporn, and Enrico Gratton. sideSPIM selective plane illumination based on a conventional inverted microscope. *Biomed. Opt. Express*, 8(9):3918–3937, sep 2017.

[29] Chris Xu and Watt W Webb. Multiphoton excitation of molecular fluorophores and nonlinear laser microscopy. In *Topics in fluorescence spectroscopy*, pages 471–540. Springer, 2002.

[30] Max Born and Emil Wolf. *Principles of optics: electromagnetic theory of propagation, interference and diffraction of light*. Elsevier, 2013.

[31] T. Sean Ross. Limitations and applicability of the Maréchal approximation. *Applied Optics*, 48(10):1812–1818, 2009.

[32] E. J. Botcherby, R. Juškaitis, M. J. Booth, and T. Wilson. An optical technique for remote focusing in microscopy. *Optics Communications*, 281(4):880–887, 2008.

[33] Mantas Žurauskas, Oliver Barnstedt, Maria Frade-Rodriguez, Scott Waddell, and Martin J. Booth. Rapid adaptive remote focusing microscope for sensing of volumetric neural activity. *Biomedical Optics Express*, 8(10):4369, 2017.

[34] Siegfried Weisenburger, Frank Tejera, Jeffrey Demas, Brandon Chen, Jason Manley, Fraser T. Sparks, Francisca Martínez Traub, Tanya Daigle, Hongkui Zeng, Attila Losonczy, and Alipasha Vaziri. Volumetric Ca2+ Imaging in the Mouse Brain Using Hybrid Multiplexed Sculpted Light Microscopy. *Cell*, 177(4):1050–1066.e14, 2019.

[35] San Francisco, San Francisco, Moffett Field, and San Francisco. Deformable mirror - based two - photon microscopy for axial mammalian brain imaging. 2019.

[36] Na Ji, Jeremy Freeman, and Spencer L. Smith. Technologies for imaging neural activity in large volumes. *Nature Neuroscience*, 19(9):1154–1164, 2016.

[37] Martí Duocastella, Bo Sun, and Craig B. Arnold. Simultaneous imaging of multiple focal planes for three-dimensional microscopy using ultra-high-speed adaptive optics. *Journal of Biomedical Optics*, 17(5):050505, 2012.

[38] Valeria Levi, Qiao Qiao Ruan, and Enrico Gratton. 3-D particle tracking in a two-photon microscope: Application to the study of molecular dynamics in cells. *Biophysical Journal*, 88(4):2919–2928, 2005.

[39] Joey M. Jabbour, Bilal H. Malik, Cory Olsovsky, Rodrigo Cuenca, Shuna Cheng, Javier A. Jo, Yi-Shing Lisa Cheng, John M. Wright, and Kristen C. Maitland. Optical axial scanning in confocal microscopy using an electrically tunable lens. *Biomedical Optics Express*, 5(2):645, 2014.

[40] Paolo Annibale, Alexander Dvornikov, and Enrico Gratton. Electrically tunable lens speeds up 3D orbital tracking. *Biomedical Optics Express*, 6(6):2181, 2015.

[41] Sz Yuan Lee, Hsi Wen Tung, Wen Chih Chen, and Weileun Fang. Thermal actuated solid tunable lens. *IEEE Photonics Technology Letters*, 18(21):2191–2193, 2006.

[42] Peter Liebetraut, Sebastian Petsch, Wolfgang Mönch, and Hans Zappe. Tunable solid-body elastomer lenses with electromagnetic actuation. *Applied Optics*, 50(19):3268–3274, 2011.

[43] G. Beadie, M. L. Sandrock, M. J. Wiggins, R. S. Lepkowicz, J. S. Shirk, M. Ponting, Y. Yang, T. Kazmierczak, A. Hiltner, and E. Baer. Tunable polymer lens. *Optics Express*, 16(16):11847, 2008.

[44] C Liu, Y Liu, E P Perillo, A K Dunn, and H Yeh. Single-Molecule Tracking and Its Application in Biomolecular Binding Detection. *IEEE Journal of Selected Topics in Quantum Electronics*, 22(4):64–76, jul 2016.

[45] Gaddum Duemani Reddy, Keith Kelleher, Rudy Fink, and Peter Saggau. Three-dimensional random access multiphoton microscopy for functional imaging of neuronal activity. *Nature Neuroscience*, 11(6):713–720, 2008.

[46] Edward J. Botcherby, Christopher W. Smith, Michael M. Kohl, Delphine Debarre, Martin J. Booth, Rimas Juškaitis, Ole Paulsen, and Tony Wilson. Aberration-free three-dimensional multiphoton imaging of neuronal activity at kHz rates. *Proceedings of the National Academy of Sciences of the United States of America*, 109(8):2919–2924, 2012.

[47] Tsai Wen Chen, Trevor J. Wardill, Yi Sun, Stefan R. Pulver, Sabine L. Renninger, Amy Baohan, Eric R. Schreiter, Rex A. Kerr, Michael B. Orger, Vivek Jayaraman, Loren L. Looger, Karel Svoboda, and Douglas S. Kim. Ultrasensitive fluorescent proteins for imaging neuronal activity. *Nature*, 499(7458):295–300, 2013.

[48] Douglas Magde, Elliot L Elson, and Watt W Webb. Fluorescence correlation spectroscopy. II. An experimental realization. *Biopolymers*, 13(1):29–61, 1974.

[49] N O Petersen, P L Höddelius, P W Wiseman, O Seger, and K E Magnusson. Quantitation of membrane receptor distributions by image correlation spectroscopy: concept and application. *Biophysical journal*, 65(3):1135–1146, sep 1993.

[50] P. W. Wiseman, J. A. Squier, M. H. Ellisman, and K. R. Wilson. Two-photo image correlation spectroscopy and image cross-correlation spectroscopy. *Journal of Microscopy*, 200(1):14–25, 2000.

[51] Benedict Hebert, Santiago Costantino, and Paul W. Wiseman. Spatiotemporal image correlation spectroscopy (STICS) theory, verification, and application to protein velocity mapping in living CHO cells. *Biophysical Journal*, 88(5):3601–3614, 2005.

[52] Michelle A. Digman, Paul W. Wiseman, Alan R. Horwitz, and Enrico Gratton. Detecting protein complexes in living cells from laser scanning confocal image sequences by the cross correlation raster image spectroscopy method. *Biophysical Journal*, 96(2):707–716, 2009.

[53] Michelle A. Digman, Claire M. Brown, Parijat Sengupta, Paul W. Wiseman, Alan R. Horwitz, and Enrico Gratton. Measuring fast dynamics in solutions and cells with a laser scanning microscope. *Biophysical Journal*, 89(2):1317–1327, 2005.

[54] C. M. Brown, R. B. Dalal, B. Hebert, M. A. Digman, A. R. Horwitz, and E. Gratton. Raster image correlation spectroscopy (RICS) for measuring fast protein dynamics and concentrations with a commercial laser scanning confocal microscope. *Journal of Microscopy*, 229(1):78–91, 2008.

[55] Elise S Cowley, Sebastian H Kopf, Alejandro LaRiviere, Wiebke Ziebis, and Dianne K Newman. Pediatric Cystic Fibrosis Sputum Can Be Chemically Dynamic, Anoxic, and Extremely Reduced Due to Hydrogen Sulfide Formation. *mBio*, 6(4):e00767—-15, sep 2015.

[56] Dieter Worlitzsch, Robert Tarran, Martina Ulrich, Ute Schwab, Aynur Cekici, Keith C Meyer, Peter Birrer, Gabriel Bellon, Jürgen Berger, Tilo Weiss, Konrad Botzenhart, James R Yankaskas, Scott Randell, Richard C Boucher, and Gerd Döring. Effects of reduced mucus oxygen concentration in airway Pseudomonas infections of cystic fibrosis patients. *The Journal of Clinical Investigation*, 109(3):317–325, feb 2002.

[57] Mette Kolpen, Christian J Lerche, Kasper N Kragh, Thomas Sams, Klaus Koren, Anna S Jensen, Laura Line, Thomas Bjarnsholt, Oana Ciofu, Claus Moser, Michael Kühl, Niels Høiby, and Peter Ø Jensen. Hyperbaric Oxygen Sensitizes Anoxic Pseudomonas aeruginosa Biofilm to Ciprofloxacin. *Antimicrobial Agents and Chemotherapy*, 61(11):e01024—-17, nov 2017.

[58] Laura Line, Morten Alhede, Mette Kolpen, Michael Kühl, Oana Ciofu, Thomas Bjarnsholt, Claus Moser, Masanori Toyofuku, Nobuhiko Nomura, Niels Høiby, and Peter Ø Jensen. Physiological levels of nitrate support anoxic growth by denitrification of Pseudomonas aeruginosa at growth rates reported in cystic fibrosis lungs and sputum. *Frontiers in Microbiology*, 5, 2014.

[59] Kelli L Palmer, Stacie A Brown, and Marvin Whiteley. Membrane-Bound Nitrate Reductase Is Required for Anaerobic Growth in Cystic Fibrosis Sputum. *Journal of Bacteriology*, 189(12):4449–4455, jun 2007.

[60] Megan Bergkessel, David W Basta, and Dianne K Newman. The physiology of growth arrest: uniting molecular and environmental microbiology. *Nature Reviews Microbiology*, 14(9):549–562, sep 2016.

[61] Alexa Price-Whelan, Lars E P Dietrich, and Dianne K Newman. Rethinking 'secondary' metabolism: physiological roles for phenazine antibiotics. *Nature Chemical Biology*, 2(2):71–78, feb 2006.

[62] Nathaniel R Glasser, Suzanne E Kern, and Dianne K Newman. Phenazine redox cycling enhances anaerobic survival in Pseudomonas aeruginosa by facilitating generation of ATP and a proton-motive force. *Molecular Microbiology*, 92(2):399–412, apr 2014.

[63] Yun Wang and Dianne K Newman. Redox reactions of phenazine antibiotics with ferric (hydr) oxides and molecular oxygen. *Environmental science & technology*, 42(7):2380–2386, 2008.

[64] Susan Hall, Catherine McDermott, Shailendra Anoopkumar-Dukie, Amelia J McFarland, Amanda Forbes, Anthony V Perkins, Andrew K Davey, Russ Chess-Williams, Milton J Kiefel, Devinder Arora, and Gary D Grant. Cellular Effects of Pyocyanin, a Secreted Virulence Factor of Pseudomonas aeruginosa. *Toxins*, 8(8), aug 2016.

[65] Gee W Lau, Huimin Ran, Fansheng Kong, Daniel J Hassett, and Dimitri Mavrodi. Pseudomonas aeruginosa Pyocyanin Is Critical for Lung Infection in Mice. *Infection and Immunity*, 72(7):4275–4278, jul 2004.

[66] Nora L Sullivan, Dimitrios S Tzeranis, Yun Wang, Peter T C So, and Dianne Newman. Quantifying the Dynamics of Bacterial Secondary Metabolites by Spectral Multiphoton Microscopy. *ACS Chemical Biology*, 6(9):893–899, sep 2011.

[67] Viera Crosignani, Sohail Jahid, Alexander Dvornikov, and Enrico Gratton. Deep tissue imaging by enhanced photon collection. *Journal of Innovative Optical Health Sciences*, 07(05):1450034, may 2014.

[68] Kumar Perinbam, Jenu V Chacko, Anerudh Kannan, Michelle A Digman, and Albert Siryaporn. A Shift in Central Metabolism Accompanies Virulence Activation in Pseudomonas aeruginosa. *mBio*, 11(2), apr 2020.

[69] Metabolic fingerprinting of bacteria by fluorescence lifetime imaging microscopy \textbar Scientific Reports.

[70] Chiara Stringari, Amanda Cinquin, Olivier Cinquin, Michelle A Digman, Peter J Donovan, and Enrico Gratton. Phasor approach to fluorescence lifetime microscopy distinguishes different metabolic states of germ cells in a live tissue. *Proceedings of the National Academy of Sciences*, 108(33):13582–13587, aug 2011.

[71] Suman Ranjit, Leonel Malacrida, Milka Stakic, and Enrico Gratton. Determination of the metabolic index using the fluorescence lifetime of free and bound nicotinamide adenine dinucleotide using the phasor approach. *Journal of Biophotonics*, 12(11):e201900156, 2019.

[72] J R Lakowicz, H Szmacinski, K Nowaczyk, and M L Johnson. Fluorescence lifetime imaging of free and protein-bound NADH. *Proceedings of the National Academy of Sciences*, 89(4):1271–1275, feb 1992.

[73] Michelle A Digman, Valeria R Caiolfa, Moreno Zamai, and Enrico Gratton. The Phasor Approach to Fluorescence Lifetime Imaging Analysis. *Biophysical Journal*, 94(2):L14—-L16, jan 2008.

[74] Farzad Fereidouni, Arjen N Bader, and Hans C Gerritsen. Spectral phasor analysis allows rapid and reliable unmixing of fluorescence microscopy spectral images. *Optics Express*, 20(12):12729–12741, jun 2012.

[75] Alexander Vallmitjana, Alexander Dvornikov, Belen Torrado, David M Jameson, Suman Ranjit, and Enrico Gratton. Resolution of 4 components in the same pixel in FLIM images using the phasor approach. *Methods and Applications in Fluorescence*, 8(3):35001, apr 2020.

[76] David M Jameson, Vickey Thomas, and DeMing Zhou. Time-resolved fluorescence studies on NADH bound to mitochondrial malate dehydrogenase. *Biochimica et Biophysica Acta (BBA)-Protein Structure and Molecular Enzymology*, 994(2):187–190, 1989.

[77] Cajetan Neubauer, Ajay S Kasi, Nora Grahl, Alex L Sessions, Sebastian H Kopf, Roberta Kato, Deborah A Hogan, and Dianne K Newman. Refining the Application of Microbial Lipids as Tracers of Staphylococcus aureus Growth Rates in Cystic Fibrosis Sputum. *Journal of Bacteriology*, 200(24), dec 2018.

[78] Sebastian H Kopf, Alex L Sessions, Elise S Cowley, Carmen Reyes, Lindsey Van Sambeek, Yang Hu, Victoria J Orphan, Roberta Kato, and Dianne K Newman. Trace incorporation of heavy water reveals slow and heterogeneous pathogen growth rates in cystic fibrosis sputum. *Proceedings of the National Academy of Sciences*, 113(2):E110—-E116, jan 2016.

[79] John A Ciemniecki and Dianne K Newman. The Potential for Redox-Active Metabolites To Enhance or Unlock Anaerobic Survival Metabolisms in Aerobes. *Journal of Bacteriology*, 202(11), may 2020.

[80] Marvin Whiteley, Kimberly M Lee, and E P Greenberg. Identification of genes controlled by quorum sensing in Pseudomonas aeruginosa. *Proceedings of the National Academy of Sciences*, 96(24):13904–13909, nov 1999.

[81] Eric Déziel, François Lépine, Sylvain Milot, Jianxin He, Michael N Mindrinos, Ronald G Tompkins, and Laurence G Rahme. Analysis of Pseudomonas aeruginosa 4-hydroxy-2-alkylquinolines (HAQs) reveals a role for 4-hydroxy-2-heptylquinoline in cell-to-cell communication. *Proceedings of the National Academy of Sciences*, 101(5):1339–1344, feb 2004.

[82] James F Parsons, Bryan T Greenhagen, Katherine Shi, Kelly Calabrese, Howard Robinson, and Jane E Ladner. Structural and Functional Analysis of the Pyocyanin Biosynthetic Protein PhzM from Pseudomonas aeruginosa. *Biochemistry*, 46(7):1821–1828, feb 2007.

[83] Martin Eschbach, Kerstin Schreiber, Katharina Trunk, Jan Buer, Dieter Jahn, and Max Schobert. Long-Term Anaerobic Survival of the Opportunistic Pathogen Pseudomonas aeruginosa via Pyruvate Fermentation. *Journal of Bacteriology*, 186(14):4596–4604, jul 2004.

[84] Nathaniel R Glasser, Benjamin X Wang, Julie A Hoy, and Dianne K Newman. The pyruvate and α-ketoglutarate dehydrogenase complexes of Pseudomonas aeruginosa catalyze pyocyanin and phenazine-1-carboxylic acid reduction via the subunit dihydrolipoamide dehydrogenase. *Journal of Biological Chemistry*, page jbc.M116.772848, feb 2017.

[85] Theerthankar Das, Samuel K Kutty, Naresh Kumar, and Mike Manefield. Pyocyanin Facilitates Extracellular DNA Binding to Pseudomonas aeruginosa Influencing Cell Surface Properties and Aggregation. *PLoS ONE*, 8(3), mar 2013.

[86] Scott H Saunders, C M Edmund, Matthew D Yates, Fernanda Jiménez Otero, Scott A Trammell, Eric D A Stemp, Jacqueline K Barton, Leonard M Tender, and Dianne K Newman. Extracellular DNA promotes efficient extracellular electron transfer by pyocyanin in Pseudomonas aeruginosa biofilms. *bioRxiv*, 2019.

[87] Suman Ranjit, Leonel Malacrida, David M Jameson, and Enrico Gratton. Fit-free analysis of fluorescence lifetime imaging data using the phasor approach. *Nature Protocols*, 13(9):1979–2004, sep 2018.

[88] Jenu V Chacko and Kevin W Eliceiri. Autofluorescence lifetime imaging of cellular metabolism: Sensitivity toward cell density, pH, intracellular, and intercellular heterogeneity. *Cytometry Part A*, 95(1):56–69, 2019.

[89] Ning Ma, Michelle A Digman, Leonel Malacrida, and Enrico Gratton. Measurements of absolute concentrations of NADH in cells using the phasor FLIM method. *Biomedical Optics Express*, 7(7):2441–2452, jul 2016.

[90] Bei Gao, Tara Gallagher, Ying Zhang, Mona Elbadawi-Sidhu, Zijuan Lai, Oliver Fiehn, and Katrine L Whiteson. Tracking polymicrobial metabolism in cystic fibrosis airways: Pseudomonas aeruginosa metabolism and physiology are influenced by Rothia mucilaginosa-derived metabolites. *mSphere*, 3(2):e00151—-18, apr 2018.

[91] Gohain Neelakshi. *Studies on the structure and function of phenazine modifying enzymes PhzM and PhzS involved in the biosynthesis of pyocyanin*. Department of Chemistry, University of Dortmund, 2008.

[92] A simplicial homology algorithm for Lipschitz optimisation \textbar SpringerLink. 72:181–217, 2018.

[93] Viera Crosignani, Alexander Dvornikov, Jose S Aguilar, Chiara Stringari, Robert Edwards, William W. Mantulin, and Enrico Gratton. Deep tissue fluorescence imaging and in vivo biological applications. *Journal of Biomedical Optics*, 17(11):116023, 2012.

[94] T. R. O'Meara. The multidither principle in adaptive optics. *Journal of the Optical Society of America*, 67(3):306, 1977.

[95] J. R. Fienup. Phase-retrieval algorithms for a complicated optical system. *Applied Optics*, 32(10):1737, 1993.

Appendix A

Appendix

A.1 Supplementary Material

Acronyms/Abbreviations:

- AO = Adaptive Optics
- AOM = Acousto-Optic Modulator
- DIVER = Deep Imaging Via Enhanced photon Recovery
- DM = Deformable Mirror
- GVD = Group Velocity Dispersion
- MPM = MultiPhoton Microscopy
- PMT = PhotoMultiplier Tube
- SHG, THG = Second Harmonic Generation, Third Harmonic Generation
- 2PEF = Two Photon Excitation Fluorescence
- FLIM = Fluorescence Lifetime Imaging Microscopy
- HIM = Hyperspectral Imaging Microscopy

A.2 AO DIVER Instrumentation

The DIVER microscope

The DIVER is designed specifically for deep tissue imaging, but can be used for any multiphoton imaging purpose. There are two detectors on the DIVER: one epi-PMT for detecting back reflected light, and one transmission PMT, the DIVER PMT, to detect signals that pass through the sample.

To improve signal acquisition in tissue, the DIVER uses a wide area photocathode PMT located beneath the sample. The transmission geometry of the DIVER means that as imaging depth is increased, the distance from the focal volume to the detector is decreasing. This implies that the numerical aperture for detection increases as a function of depth and the fluorescence signal travels through less tissue, meaning that it is less likely to be absorbed or scattered before detection. A filter wheel contains several bandpass filters to select specific fluorescence signals. Above and below the filter wheel there are two BG-39 filters that effectively block out all excitation light from the PMT. To further improve light collection, the BG-39 filters and the filter wheel are submerged in an index matching fluid. Index matching ensures maximum signal throughput from the sample to the detector.

AO instruments

The adaptive element we used is a deformable mirror (DM) from Boston Micromachines. The DM consists of 37 hexagonal mirror segments, each segment measuring just a few microns across. Each segment is controlled independently of the rest of the mirror using three micro-electromechanical actuators. The three actuators allow precise (12 nanometer-scale) control of the piston, tip, and tilt of each segment. The overall shape of the DM can be updated at a rate of about 10,000 adjustments per second, allowing rapid corrections to be made while the microscope is scanning through a sample.

We also used a HASO4 wavefront sensor on loan from Imagine Optic. The wavefront sensor is a Shack-Hartmann type and is calibrated for 680-900nm light.

A.3 Alternative adaptive optics techniques

A.3.1 Direct wavefront sensing

A technique to quantify how the medium is affecting the image is to use a guide star and image it with a wavefront sensor. In astronomy, a guide star can be a star in the field of view of the telescope, or it can be created artificially by focusing a laser beam into the sodium layer in the atmosphere at an altitude of about 100km. The guide star produces a reference point that is used to set the adaptive element.

In microscopy, guide stars are typically created by illuminating fluorescent beads to produce spherical wavefronts that are then imaged onto a wavefront sensor. In deep tissue imaging, it is difficult and sometimes impossible to directly measure the wavefront. This is because the wavefront is measured by light that has to propagate from a point source (guide star) up through the sample, then through a microlens to a CCD or CMOS camera. The deviation of the focal points from each microlens from the center of the field of view is a measure of the tip/tilt at that region in wavefront. The deformable mirror is then set to the exact opposite shape of the measured wavefront to minimize the phase variation on the back focal plane of the objective, ϕ_{BF}. This method works well as long as the light in the sub aperture is spatially coherent, meaning that the spatial variation in the wavefront is fairly small so that a small focal point can be formed by each microlens. When the guide star is too deep or dim, then signal in the wavefront sensor is washed out by noise. If the sample is too scattering, then the phase varies too rapidly over the aperture of the microlens and the focus is too distorted and smeared out to extract meaning.[22] Direct wavefront sensing will not work for deep tissue imaging at the depths that the DIVER can image because the sensor

cannot collect enough spatially coherent fluorescent light.

Coherent Optical Adaptive Techniques: COAT

One class of techniques we plan to explore for the AO DIVER is known as Coherent Optical Adaptive techniques or COAT. A simulation has been programmed into SimFCS but is not yet complete. This is based on the assumption that the light waves used to detect or image a system are coherent, and so any changes in the phase of neighboring mirror segments (or neighboring radiation sources) will result in interference patterns. The interference effects of coherent light allows us to encode phase relationships in the focal volume into intensity variations. One of the COAT applications is the multidither principle [94]. In one version of the multidither principle, an array of mirrors is oscillated, each mirror with its own fundamental frequency, ω_i. The oscillating mirrors produce an interference pattern that is amplitude modulated at the same frequency as the phase modulation. Each mirror's phase modulation is then directly mapped into the intensity modulation at the same frequency. The amplitude modulation signal is then detected with a fast detector that does not need to resolve the actual interference pattern. The signal is broken into its frequency components using a synchronous detector that is driven by the dither oscillator. Low frequency variations in the signal at each frequency are then fed back into the phase of each mirror. This results in a "hill climbing" behavior that pushes the mirror into phase with its neighbors.

Phase retrieval algorithms

Phase retrieval algorithms find application in a variety of different fields, such as x-ray crystallography, laser pulse shaping, holography, and it is being explored as a tool for imaging systems engineering [95].

The Gerchberg-Saxton phase retrieval algorithm is an iterative algorithm which takes as input the intensity distribution of the laser beam profile, I_m, and the resulting image, $\tilde{I}_m$. The GS algorithm

is shown schematically in Figure A.1.

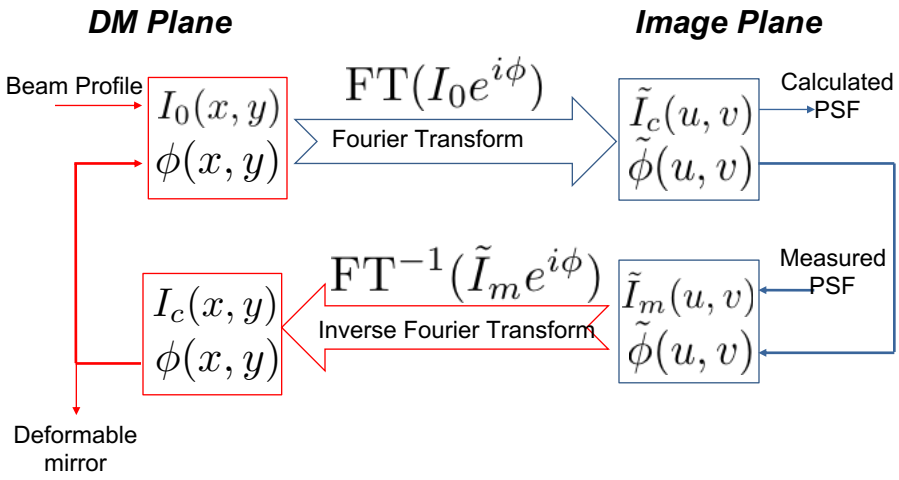

Figure A.1: The Gerchberg-Saxton Algorithm

The pseudocode for the algorithm is:

```
Gerchberg - Saxton Algorithm(Source, PSF, Retrieved_Phase)
 A = IFT(Target)
 while error criterion is not satisfied
   B = Amplitude(Source) * exp(i*Phase(A))
   C = FT(B)
   D = Amplitude(PSF) * exp(i*Phase(C))
   A = IFT(D)
 end while
 Retrieved_Phase = Phase(A)
end Gerchberg - Saxton Algorithm
```

The algorithm works by minimizing the difference between the actual PSF and the calculated PSF by changing only the phase applied to the source. Once the difference between the calculated PSF and the measured PSF is small enough, the best guess for the phase is returned from the function.

The phase now describes the aberrations in the image after propagation through the tissue. The algorithm returns the principal components of the complex field, meaning that the phase will be between $-\pi$ and π. If the aberrations are large, it is likely that the physical phase will be far outside this range. The resulting phase map will have discontinuous jumps because of the $n\pi$ ambiguity, known as "phase wrapping". To accurately set the mirror so that we do not have diffraction peaks blurring the image, we need to unwrap the phase by adding appropriate integer multiples of π. Finally, the calculated phase must be applied to the deformable mirror. This is done by numerically projecting the phase onto the hexagonal segments of the mirror. To do this, the unwrapped phase map is multiplied by hexagonal pupil functions. The average value of the phase in the segment is calculated using the formula

$$p_i = a_i \int\int \phi_{\text{retrieved}}(x,y) \cdot \text{HexPupil}_i(x,y) dxdy \tag{A.1}$$

and the x and y tilts at each segment i are calculated using the formula

$$\text{x-tilt}_i = a_i \int\int \text{x} \cdot \phi_{\text{retrieved}}(x,y) \cdot \text{HexPupil}_i(x,y) dxdy \tag{A.2}$$

$$\text{y-tilt}_i = a_i \int\int \text{y} \cdot \phi_{\text{retrieved}}(x,y) \cdot \text{HexPupil}_i(x,y) dxdy \tag{A.3}$$

Where a_i is a factor used to normalize the Zernike integrals over a hexagonal pupil instead of a circular pupil.

A.3.2 Phase retrieval progress

The phase retrieval algorithm is implemented in Matlab. The results depend on the initial aberration, but in the case shown in Figure A.2, the ratio between the area at half maximum of the diffraction limited PSF and the corrected PSF is 0.999, and the sum of the differences between initial aberrated PSF and the approximation to the aberrated PSF drops from 10% to about 0.7%.The

algorithm has not yet been implemented in the AO DIVER system.

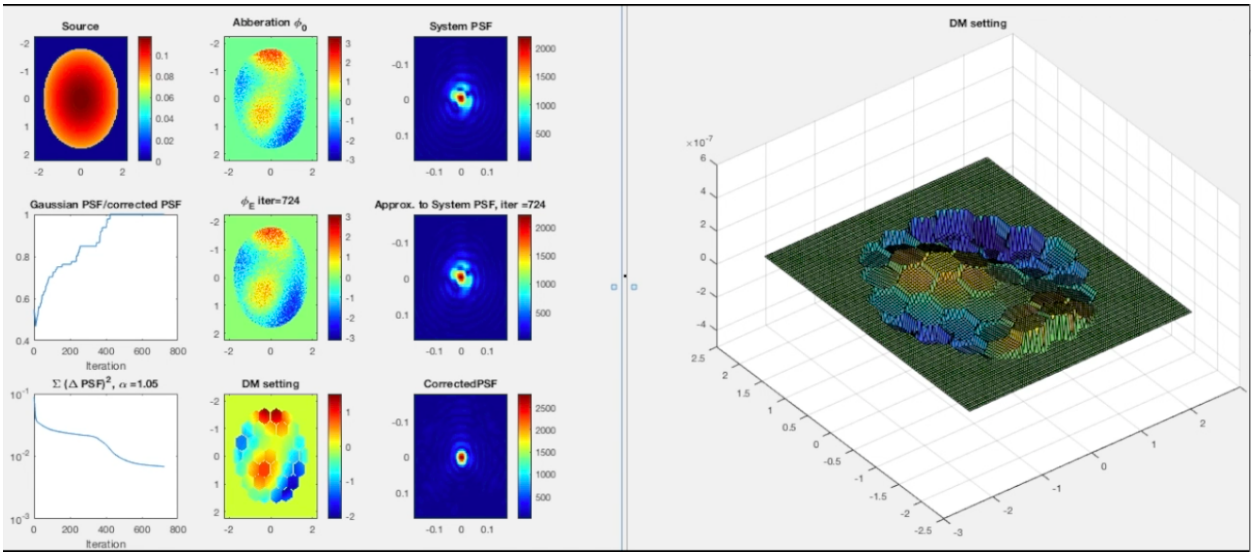

Figure A.2: Phase retrieval simulation in Matlab. From top left, we have the theoretical beam profile, then initial aberration in the system ϕ_0. The resulting system PSF is shown next to the aberration. The closest approximation to the aberration and the system PSF are shown in the second row. The wavefront is then projected onto the DM model, and subtracted from the system aberration. The final resulting PSF is shown on the bottom right. The large image on the right is the topography of the DM with the wavefront correction.

A.4 The phasor

The phasor approach to FLIM and HIM is a method to represent the temporal and spectral characteristics of each pixel in the image as the coefficients of the Fourier transform. Each harmonic, n, of the phasor represents a coefficient in the Fourier series,

$$f(x) = \frac{1}{2}a_0 + \sum_{n=1}^{\infty} g_n \cos(2\pi n x) + \sum_{n=1}^{\infty} s_n \sin(2\pi n x). \tag{A.4}$$

The coefficients are calculated by the integrals,

$$s(n) = \frac{\int_{T_0}^{T_1} I(t)\sin(2\pi n\frac{t-T_0}{T_1-T_0})dt}{\int_{T_0}^{T_1} I(t)dt} \tag{A.5}$$

$$g(n) = \frac{\int_{T_0}^{T_1} I(t)\cos(2\pi n\frac{t-T_0}{T_1-T_0})dt}{\int_{T_0}^{T_1} I(t)dt} \tag{A.6}$$

For each harmonic, n, the coefficients can be plotted on a cartesian coordinate system. The orthogonality of the sine and cosine basis functions ensures that s and g are independent measurements, and each harmonic of each s and g are independent. In Fig. A.3 the Fourier series approximation to a Gaussian function are shown. The power in each frequency is shown, as well as the location on the phasor plot of each harmonic s and g.

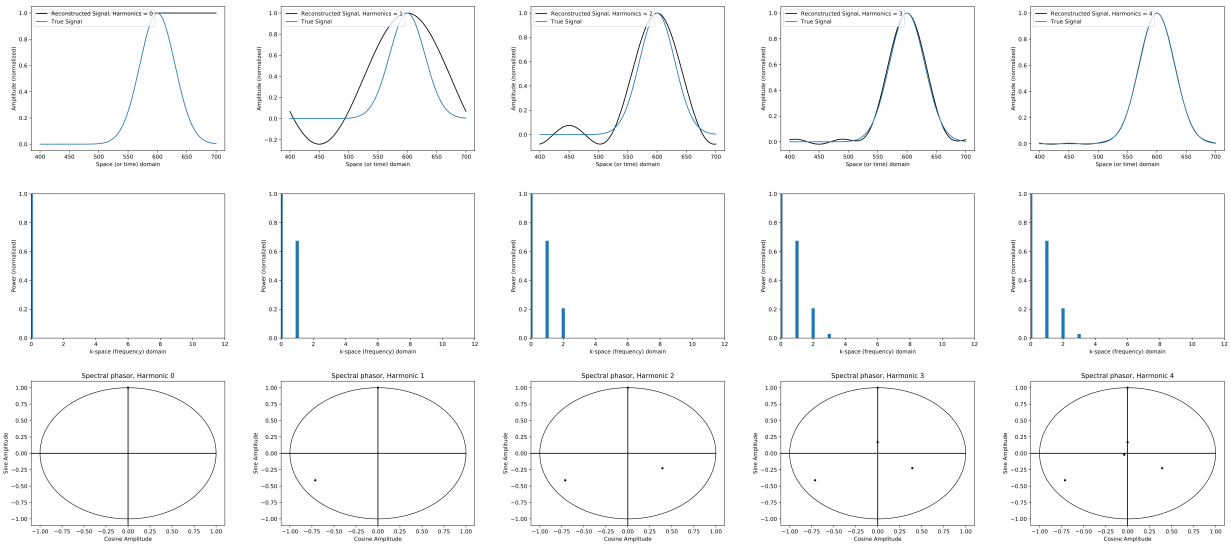

Figure A.3: Fourier Series approximation to a Gaussian function. Higher harmonics improve the series approximation to the function.

For any arbitrary linear combination of k functions with phasor coefficients s_i, g_i, the coefficients of the Fourier series of the combination, s and g, will be a linear combination of the pure species s_i, g_i. To un-mix the species, a system of equations can be set up in the form $AX = B$:

$$\begin{bmatrix} s_{1,1} & \cdots & s_{1,k} \\ g_{1,1} & \cdots & g_{1,k} \\ \vdots & \ddots & \\ s_{n,1} & \cdots & s_{n,k} \\ g_{n,1} & \cdots & g_{n,k} \end{bmatrix} \begin{bmatrix} f_1 \\ \vdots \\ \vdots \\ f_k \end{bmatrix} = \begin{bmatrix} s_1 \\ g_1 \\ \vdots \\ s_n \\ g_n \end{bmatrix}$$

With the constraint that

$$\sum_{i=1}^{k} f_i = 1 \tag{A.7}$$

If the matrix A is square it can be inverted, but in most cases, the system will be under or over determined. For these cases the system is written in a least squares form,

$$\vec{f} = \text{argmin}_f \left\{ \sum_n \left(S_{\text{model}}(\vec{f}, n) - S_{\text{signal}}(n) \right)^2 + \sum_n \left(G_{\text{model}}(\vec{f}, n) - G_{\text{signal}}(n) \right)^2 \right\} \tag{A.8}$$

In Fig. A.4, a simulated signal is generated with 6 contributing single exponential decays, in other words there are 6 unknown fractional contributions. With one harmonic, there are three known constraints: the signal s, and g, and the constraint that all fractions add to 1. With two harmonics, there are 5 constraints: the signal s_1, and g_1, s_2, and g_2 and the constraint on the fractional contributions. Despite being under-determined, the error in the unmixing algorithm is negligible.

Python code used to unmix LSM and R64 files can be found at https://github.com/swleemans/HyperFluo.

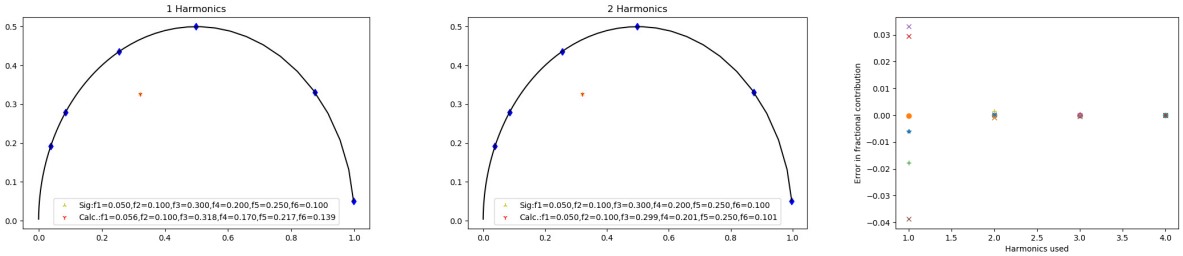

Figure A.4: A system of 6 FLIM species can be unmixed with some error using only one harmonic, but has almost perfect results in simulations using two harmonics, despite the system being underdetermined.